TECHNISCHE UNIVERSITÄT
ILMENAU

PUCP

Synthesis of Hydroxyapatite thin films on PMMA Printed Substrates

Student: Yesenia Haydee Sauñi Camposano

Thesis submitted for the degree of Master of Science in Material Science and Engineering

Advisor, Ilmenau:

Univ.-Prof. Dr.-Ing. habil. Edda Rädlein

Dr. Ing. Rolf Grieseler

Advisor, Lima:

Dr. Ing. Francisco Rumiche

October 2017, Ilmenau

Statement

Hereby, I declare that I have elaborated the present work without any non-specified assistance. The people involved on this research, literature, as well as any other resource used in this thesis have been completely specified throughout and the end of the text.

27th November 2017, Ilmenau

Yesenia Haydee Sauñi camposano

Dedication

To my mother Julia Capcha and my sisters that with their support, encouragement, and constant love have sustained me throughout my life.

Acknowledgements

I want to thank God for allowing me to complete this stage of my life with the elaboration of this work, for the strength that gives us day by day and for guiding my life.

I would like to thank the institutes that allowed me to finish this work. To the financing provided by CONCYTEC under the program: “Becas concytec para maestrias 2015-2”. To the TU-Ilmenau and PUCP for providing me with the dual degree program that allowed me to perform my master studies.

I am deeply grateful to my supervisors, Prof. Edda Rädlein , Dr. Francisco Rumiche and Dr. Rolf Grieseler for all the support provided during the development of this investigation and for their kind guidance.

To the staff of the Digital Manufacturing Room (VEO) of the PUCP for their constant support and interest in the development of this work providing materials and equipment.

Many thanks are given to Msc. Honig Hauke and Ing. Michael Fischer for their help and guidance to perform the tests required for this work. Also to a colleague and friend Ing. Alfonso Ugarte for all his help and collaboration in the development of this project.

Thanks to Aissa Muños for her support in the process coating substrates in the Laboratory of Materials Science of the PUCP.

Finally I appreciate the motivation, encouragement and constant support of my family and friends, especially Miguel Fernadez, who encouraged me to start this challenge.

Contents

List of figures

Abstract

Each year millions of people suffer from bone defects resulting from trauma, tumors or bone-related injuries. Therefore there is a need to continuously develop new materials or improve the properties of the materials currently used, for bone replacement or implant applications. Polymethyl methacrylate (PMMA) has proven to be a promising alternative as a material for implants; however, there are still some limitations inherent to this material, particularly related to its surface properties.

This thesis work is focused on the fabrication of hydroxyapatite (HAp) thin films on the surface of 3D printed PMMA substrates. 3D printing, particularly the Fused Deposition Modeling (FDM) technique was used to fabricate PMMA substrates with different surface porosity levels. FDM technique exhibits the potential for fabricating customized freeform structures for several applications including craniofacial reconstruction. HAp thin films were deposited by Radio Frequency Magnetron Sputtering (RFMS) and Ion Beam Sputtering (IBS) techniques, with a commercial target and an "in house" sintered target, respectively. A structural, chemical, mechanical, and morphological characterization was conducted in the generated surfaces by means of X-ray diffraction (XRD), scanning electron microscopy (SEM), energy dispersive spectroscopy (EDS), and hardness and roughness measurements.

The results of the XRD analysis revealed an amorphous structure for the films produced by both RFMS and IBS techniques on the PMMA substrates. The micrographs obtained by SEM showed a columnar morphology and a low density for the films produced by RFMS; the same technique revealed a structure of ridges of standing platelets with curved contours for the IBS deposited films. The amorphous structure and the morphology of the films, as well as the hardness and roughness can be propitious to improve surface properties and promote the osseointegration capabilities of PMMA.

This work contributes to the basis for the development of a PMMA implant manufacturing process using 3D printing and HAp film deposition techniques, with improved osseointegration properties.

Resumen

Cada año, millones de personas sufren defectos óseos como resultado de traumas, tumores o lesiones relacionadas con los huesos. Por lo tanto, existe la necesidad de desarrollar continuamente nuevos materiales o mejorar las propiedades de los materiales utilizados actualmente, para aplicaciones de reemplazo óseo o implantes. El polimetilmetacrilato (PMMA) ha demostrado ser una alternativa prometedora como material para implantes; sin embargo, todavía existen algunas limitaciones inherentes a este material, particularmente relacionadas con sus propiedades superficiales.

Este trabajo de tesis se centra en la fabricación de películas delgadas de hidroxiapatita (HAp) en la superficie de sustratos de PMMA impresos en 3D. La impresión 3D, particularmente la técnica de modelado de deposición fundida (FDM), se utilizó para fabricar sustratos de PMMA con diferentes niveles de porosidad superficial. La técnica FDM exhibe el potencial para fabricar estructuras personalizadas de para varias aplicaciones, incluida la reconstrucción craneofacial. Las películas delgadas de HAp se depositaron mediante técnicas de deposición catódica con Magnetrón y radio frecuencia (RFMS) y deposición catódica con haz de iones (IBS), con un target comercial y un target sinterizado "in house", respectivamente. Se realizó una caracterización estructural, química, mecánica y morfológica en las superficies generadas por medio de difracción de rayos X (XRD), microscopía electrónica de barrido (SEM), espectroscopía de energía dispersiva (EDS) y medidas de dureza y rugosidad.

Los resultados del análisis de XRD revelaron una estructura amorfa para las películas producidas por ambas técnicas RFMS e IBS en los sustratos de PMMA. Las micrografías obtenidas por SEM mostraron una morfología columnar y una baja densidad para las películas producidas por RFMS; la misma técnica reveló una estructura de crestas de plaquetas con contornos curvados para las películas depositadas IBS. La estructura amorfa y la morfología de las películas, así como la dureza y la rugosidad pueden ser propicias para mejorar las propiedades de la superficie y promover las capacidades de oseointegración del PMMA.

Este trabajo contribuye a la base para el desarrollo de un proceso de fabricación de implantes de PMMA usando impresión 3D y técnicas de deposición de película HAp, con propiedades mejoradas de oseointegración.

Zusammenfassung

Jedes Jahr leiden Millionen von Menschen an Knochendefekten infolge von Traumata, Tumoren oder knochenbedingten Verletzungen. Daher besteht die Notwendigkeit, ständig neue Materialien zu entwickeln oder die Eigenschaften der derzeit verwendeten Materialien für Knochenersatz oder Implantatanwendungen zu verbessern. Polymethylmethacrylat (PMMA) hat sich als Material für Implantate als vielversprechende Alternative erwiesen; Es gibt jedoch immer noch einige Einschränkungen, die diesem Material inhärent sind, insbesondere in Bezug auf seine Oberflächeneigenschaften.

Diese Arbeit konzentriert sich auf die Herstellung von Hydroxylapatit (HAp) -Dünnfilmen auf der Oberfläche von 3D-gedruckten PMMA-Substraten. Das 3D-Printing, insbesondere das FDM-Verfahren (Fused Deposition Modeling), wurde zur Herstellung von PMMA-Substraten mit unterschiedlichen Oberflächenporositätsgraden verwendet. Die FDM-Technik weist das Potential zur Herstellung von maßgeschneiderten Freiformstrukturen für verschiedene Anwendungen auf, einschließlich der kraniofazialen Rekonstruktion. HAp-Dünnfilme wurden mittels Radiofrequenz-Magnetron-Sputtern (RFMS) und Ionenstrahl-Sputtern (IBS) -Techniken mit einem kommerziellen Target bzw. einem "in-house" gesinterten Target abgeschieden. Eine strukturelle, chemische, mechanische und morphologische Charakterisierung wurde in den erzeugten Oberflächen mittels Röntgenbeugung (XRD), Rasterelektronenmikroskopie (REM), energiedispersiver Spektroskopie (EDS) und Härte- und Rauheitsmessungen durchgeführt.

Die Ergebnisse der XRD-Analyse zeigten eine amorphe Struktur für die Filme, die sowohl durch RFMS- als auch IBS-Techniken auf den PMMA-Substraten hergestellt wurden. Die durch SEM erhaltenen mikroskopischen Aufnahmen zeigten eine Säulenmorphologie und eine niedrige Dichte für die durch RFMS hergestellten Filme; Die gleiche Technik zeigte eine Struktur von Stegen von stehenden Plättchen mit gekrümmten Konturen für die abgeschiedenen IBS-Filme. Die amorphe Struktur und die Morphologie der Filme sowie die Härte und Rauheit können günstig sein, um die Oberflächeneigenschaften zu verbessern und die Osseointegrationsfähigkeiten von PMMA zu fördern.

Diese Arbeit leistet einen Beitrag zur Entwicklung eines PMMA-Implantationsherstellungsverfahrens unter Verwendung von 3D-Druck- und HAp-Filmdepositionstechniken mit verbesserten Osseointegrationseigenschaften.

Introduction

Motivation

Craniofacial defects represent alterations in the anatomy and morphology of the skull or craniofacial bone as a result of trauma, tissue necrosis associated with infections, or defects caused by surgical procedures [1]. In order to correct these defects, manufacture of reconstruction structures is conducted with many techniques and technologies, including methods where alloplastic implant materials are used. Currently, the most widely used alloplastic material for craniomaxillofacial reconstruction is methyl polymethacrylate (PMMA), a biocompatible and non-degradable resin-based acrylic material, which can be fabricated as an implant prior to surgery, with the advantages of reduced surgical time , the use of a simple technique, and excellent aesthetics with long-term results [2].

Bone is a natural organic-inorganic ceramic compound and contains about 70% by weight of calcium phosphate, which is regularly dispersed in a collagen fibril matrix. The calcium phosphate embedded in bone has the form of nano-crystals, the nanoparticles that it presents in its crystalline structure is hydroxyapatite (HAp), with the chemical formula $Ca_{10}(OH)_2(PO_4)_6$ [3]. As a result, synthetic HAp has been extensively investigated as a substitute or replacement for bone in biomedical applications [4], allowing it to exploit its versatile combination with other materials to obtain a material with desired properties for specific applications [5].

3D printing has become an attractive route for the development of biocompatible materials in relatively short times [6]. In recent years, there have been many reports on the manufacture of scaffolds for bone tissue engineering with 3D printing and on critical factors and process parameters [7].

This thesis focuses on the manufacture of thin films of hydroxyapatite (HAp), by cathodic deposition, on the surface of PMMA substrates printed in 3D. The technique of 3D printing used in the investigation was fused deposition modeling (FDM); PMMA substrates with different levels of surface porosity were generated. The mechanical properties of the films and the interaction with the substrate was evaluated. It i expected that, both, the porous structure and the chemical composition of HA thin films, enhance the PMMA osseointegration properties. This configuration will generate a better alternative for craniofacial implants.

General objective

To fabricate and characterize thin films of hydroxyapatite on PMMA substrates printed with 3D technology.

Specific objectives

- To produce PMMA substrates with different level of porosity through the 3D printing process (FDM).
- To deposit thin films of hydroxyapatite on the PMMA substrates by RF magnetron sputtering (RFMS) and ion beam sputtering (IBS) deposition.
- To characterize the thin films using techniques that allow to evaluate the structure, chemical composition, and morphology.

1 State of technology

1.1 Hydroxyapatite (HAp)

Hydroxyapatite is one of the many types of calcium phosphate (CaP) that belongs to the family of apatites. The apatite family is formed by a number of elements characterized by having similar crystallographic structures but not necessarily identical compositions. Table 1 shows some of the existing calcium phosphate phases [8]. Out of these phases , the crystalline HAp shows the slowest degradation rate, compared with other calcium phosphates, making it the type most commonly used for medical applications [9], The dissolution rate decreases as follows [8][10]:

ACP» α-TCP » β-TCP » TTCP » OA » HAp

Table 1: Some Calcium phosphate phases [8]

Phase	Chemical Formula	Symbol	Solubility Constant	Ca/P ratio
Hydroxyapatite	$Ca_{10}(PO_4)_{6(}OH)_2$	HAp	$6.62x10^{-126}$	1.67
Amorphous calcium phosphate		ACP		
α-Tricalcium phosphate	α-$Ca_3(PO_4)_2$	α-TCP	$8.46x10^{-32}$	1.50
β-Tricalcium phosphate tetracalcium	β-$Ca_3(PO_4)_2$	β-TCP	$2.07x10^{-33}$	1.50
Tetracalcium phosphate	$Ca_4P_2O_9$	TTCP	N/A	2.00
Oxyapatite	$Ca_{10}(PO_4)_6O$	OA	$\sim10^{-69}$	1.67

HA has a specific composition: (Ca_{10} $(PO4)$ $_6$ (OH) $_2$). It has a theoretical composition of 39.68% by weight Ca, 18.45% by weight P, and a Ca/P weight ratio of 2.15 (corresponding to the Ca / P atomic ratio of 1.67) [11][10].

1.1.1 Crystal structure of hydroxyapatite

The HA has a hexagonal crystal system and in its structure has two main planes: the plane a and the plane c, as shown in Figure 1 [12].

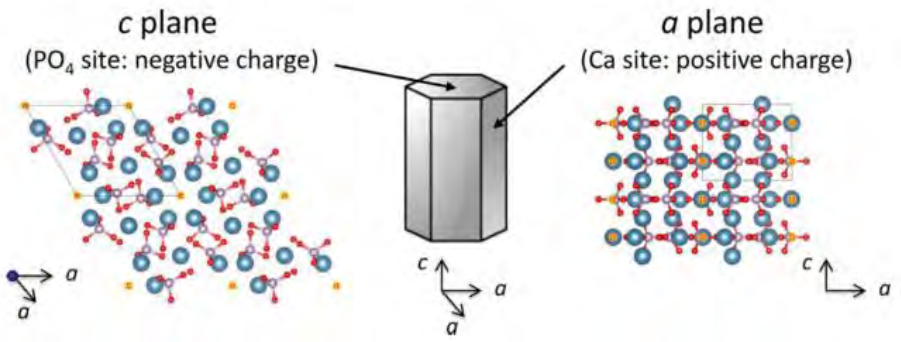

Figure 1: Crystalline structure and schematic illustration of stoichiometric hydroxyapatite. HAp contains both the cations and anions in its structure and has a high affinity for organic molecules. Circles represent: blue Ca, white P, red O and OH [12]

The Hexagonal HAp belongs to the spatial group $P6_3/m$ with lattice parameters a = b = 0.94 nm y c = 0.69 nm, and has two units of formula per unit cell. Calcium ions at site 1, Ca (I), are coordinated by nine oxygen atoms forming a polyhedron, while Ca (II) are coordinated by five oxygen atoms and a hydroxyl group forming an octahedron. The coordination number of Ca (II) ions is 7, one of which presents a weak bond to another oxygen. The hydroxyl ions are in columns parallel to the axis c, which pass through the centers of the triangles of calcium, which are in the planes of symmetry in z = 1/4 y 3/4. The atomic positions of the HAp structure and the number of atoms per unit cell are shown in Table 2. The atomic structure based on the values in Table 2 shows the complexity of the structure [13].

Table 2: Atomic positions of the hydroxyapatite structure [13]

Atom	Number of atoms per unit cell	x	y	z
Ca (I)	4	0.333	0.667	0.001
Ca (II)	6	0.246	0.993	0.250
P	6	0.400	0.369	0.250
O (I)	6	0.329	0.484	0.250
O(II)	6	0.589	0.466	0.250
O(III)	12	0.348	0.259	0.073
OH	2	0.000	0.000	0.250

The general view is that plane **a** is positively charged because it is rich in calcium ions, while plane c is rich in phosphate and hydroxide ions and therefore is negatively charged. That is, HAp surfaces exhibit anisotropic characteristics such as anisotropic adsorption profiles for biomolecules. The ion composition of the surface (and therefore the surface charge) of HAp in an aqueous medium varies according to the ion composition of the medium due to ion exchange and the gradual dissolution [12].

Mechanical and physical properties of Hydroxyapatite

The mechanical and physical properties of HAp are shown in Table 3.

Table 3: Mechanical properties of Hydroxyapatite [10]

Property	Values
Density (g/m^3)	3.15
Young modulus (GPa)	85-90
Knoop Hardness (MPa)	3450
Tensile Strength (MPa/m)	120
Poisson Coefficient	0.3
Thermal Expansion (1/K)	11
Melting Point (°C)	1660
Specific Heat (Cal.g^{-1}.K^{-1})	0.15
Thermal Conductivity (W.cm^{-1}.K^{-1})	0.01
Fracture Toughness (MPa/m)	1.0
Weibull Modulus	5.0-12.0

1.2 Sintering of Hydroxyapatite

1.2.1 Sintering of ceramics

Sintering is the process of thermal treatment, with or without application of external pressure, of a system of individual particles (metallic, ceramic, polymer) in the form of a compact porous agglomerate (work-piece), in order to transform it in a dense product that evolves to a state of maximum compaction (Reduction of porosity) and strength, as a result of the union between particles of the material [14][15]. Physical parameters, such as powder grain size distribution, specific surface area of powder or compaticity of shaped body, may change sintering ability and kinetics [15]. The process of sintering can be divided in three stages, which are described as follows:

- **First stage**

In this initial stage, also called necking stage, the particles start to join with each other, by the formation of necks. This stage can occur with a light or without densification and the macroscopic contraction of the sample it is not appreciable. A simple model of spherical particles can be used to schematize the initial powder compaction and the changes that occur at the microscopic scale during this stage (see Figure 2) [14].

- **Second stage**

This stage covers the major part of sintering, where, the necks thicken creating a three-dimensional structure, in which the particles tend to round the void spaces, forming a porous texture. Densification occurs due the shrinking of the pores and it ends when the pores pinch off to become isolated.

The most characteristic macroscopic effect in this stage of sintering is a marked contraction of the sample, which reaches almost the final value of the whole process, which results in an increase in the shrinkage [15], a schema is showed in Figure 2.

- **Third stage**

In this stage of sintering, the pores tend to get a spherical shape, losing their continuous texture and are isolated in the mass of the piece. The rate of sintering decreases and the increase in shrinkage of the workpiece is much less marked than in the previous step, to the point where it is difficult to determine exactly when the sintering process has finished. This final stage of sintering implies the elimination of the final porosity, which disappears by the diffusion of vacancies along the grain boundaries. Therefore, the pores must remain close to grain boundaries[16]. See Figure 2.

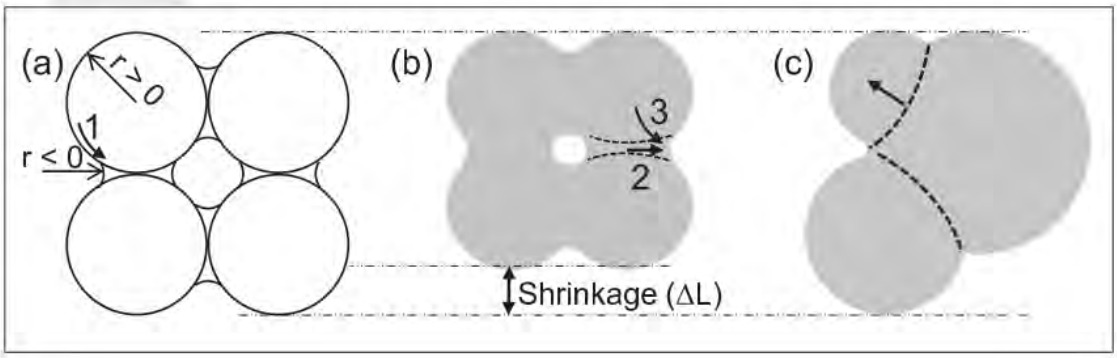

Figure 2: (a) Adjacent spheres model: consolidation by superficial diffusion (1) and formation of necks between grains. (b) Secant spheres model: consolidation and densification by volume (2) or grain boundary (3) diffusion. (c) Coalescence and grain growth by grow by grain boundary sliding [16].

1.2.2 Sintering of Hydroxyapatite

Sintering of HAp, without application of external pressure, is generally performed in the temperature range of 1100–1250 °C. In this domain, densification occurs without formation of any liquid phase [16]. However C. Yang et al. sintered HAp at different temperatures (1200, 1250, 1300, 1350 °C), in all of them the HAp was decomposed into β-TCP. The decomposition ratio increased with ascent of sintering temperature, as shown in Figure 3, where it is observed that the highest rate of decomposition (80%) occurs when the sintering is carried out at 1 350 ℃ [17].

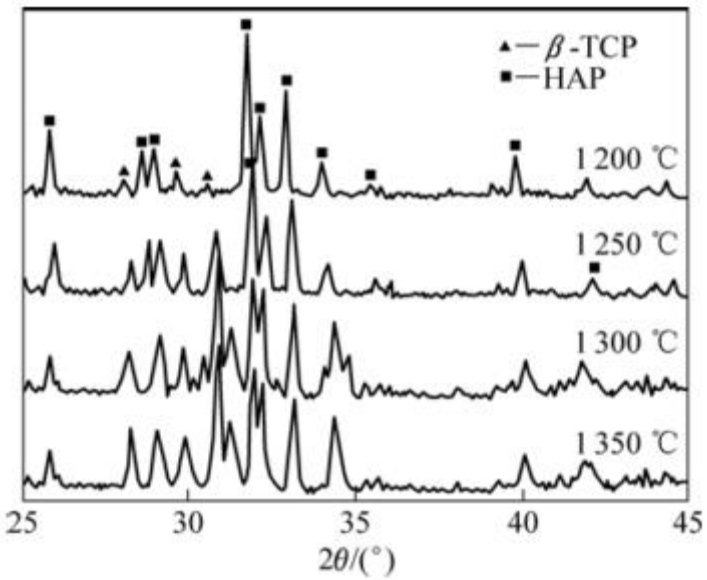

Figure 3: XRD patterns of HAp ceramics sintered at different temperatures for 2 hours [17]

It is important to take into account the thermal stability of HAp, which can be dived in stages. In a temperature range of 25 to 200 °C adsorbed water is reversibly removed from HAp, lattice water is irreversibly removed between 200 and 400 °C, due to the loss of lattice water a contraction occurs in the lattice dimension of HAp. Surface phosphorus is reactive and will readily form a P-OH that is dehydroxylated above 400 °C, to form P-O-P surface groups [18].

Phase transformation of HAp consists in two processes: dehydroxylation and decomposition[16][19]. Dehydroxylation of HAp begins at temperatures at about 900 °C in air and 850 °C in a water-free atmosphere[18]. HAp gradually loses OH ions at elevated temperature and turns to oxyhydroxyapatite, according to a reversible reaction [16][19] [18].

$$Ca_{10}(PO_4)_6(OH)_2 \rightarrow Ca_{10}(PO_4)_6(OH)_{2-2x}O_x\blacksquare_x + xH_2O \quad (1)$$

where $\blacksquare_x$ is a hydrogen vacancy.

In the range of 900 °C-1350 °C reversible dehydroxylation is accompanied by HAp decomposition, which is a process of continuous reactions [18] [19]. HAp can decompose into calcium phosphate ($\alpha - TCP$), β -calcium phosphate ($\beta - TCP$) and calcium oxide (CaO) according to the reaction in Equation 2 [19].

$$Ca_{10}(PO_4)_6(OH)_2 \rightarrow 2Ca_3(PO_4)_2 + Ca_3(P_2O_8)_6 + CaO + H_2O \quad (2)$$

The dehydroxylation and decomposition of HAp in the sintering process have been studied [20], concluding that by preventing the loss of (OH^-) it is possible to suppress decomposition.

1.3 Hydroxyapatite thin films

In order to improve the surface properties of some materials used for osseous implants, HAp is often applied as thin coatings, in particular over titanium and stainless steels or alloys [21]. Numerous techniques have been used for the deposition of HAp and Calcium Phosphate coatings [22][21]. The most relevant ones are discussed in the following sections.

1.3.1 Plasma Spraying

In this technique a plasma is generated due a stream of gases that passes through an electric arc of direct current, which is formed by two electrodes. This stream of mixed gases is ionized by this arc, with a temperature above 20000 K and a speed of up to 400 m/s. The temperature of the plasma decreases as a function of distance from the electrodes, 6 cm outside the electrodes the temperatures are around 2000–3000 K A material in powder, suspended in a carrier gas is injected into the plasma, the particles of the material are accelerated and heated in the plasma and then impact onto the substrate. Due to sudden deceleration of the flow at the point of impact, a buildup of pressure is generated at the interface particle-surface that forces the liquid material to flow laterally, thereby is formed a film with the same composition of the powder on the substrate surface. The temperature of the substrate is in a range of 100–150 °C, therefore plasma spraying is usually considered to be a cold process [22][23].

1.3.2 Vacuum plasma spraying (VPS) or low-pressure plasma spraying (LPPS)

When the plasma spraying process is performed in a chamber with a low pressure atmosphere (50– 100 mbar), it takes the name of low-pressure plasma spraying (LPPS). In a low-pressure process the reaction between the gas and the particles can be avoided or reduced and the plasma jet velocity is increased up to three times the speed of sound. Also, the plasma jet size is increased to 40–50 cm while atmospheric plasma spraying gives a plasma jet length of 4–10 cm. The advantage of this technique with respect to plasma atmospheric spraying is the good adhesion and the reduced porosity in the coating films, due to a higher speed of discharge of the material on the substrate. A disadvantage is the increase in the substrate temperature [22][24].

1.3.3 Electrophoretic deposition

This technique has been used to produce uniform Ca–P coatings on metallic substrates. This approach is especially useful for porous metal structures such as orderly oriented wire mesh [22].

Electrophoretic deposition is based on the suspension of charged particles in a solvent, these particles are attracted and deposited onto a conductive substrate of opposite charge by an application of a DC electric field. There are two types of electrophoretic deposition. Cathodic electrophoretic deposition, when particles positively charged are deposited on the cathode, and anodic electrophoretic deposition when negatively charged particles are deposited on the anode [25].

1.3.4 Sol–gel deposition

Sol–gel deposition is a method which results in ceramic coatings with an exact chemical and microstructural composition besides high density and strong adhesion to the substrate [22].

In this process the components of the coating (reagents), are mixed in solution forming a colloidal suspension of inorganic particles, as metal alkoxides or other organic precursors. The substrates are dip coated with the solution, at low reaction temperatures, and then are annealed at temperatures in the range of 400–1000 °C [22][26].

1.3.5 Electrochemical deposition

The electrochemical deposition is a method to form uniform coatings, one of its advantages is that the process is carried out at room temperature and the coating morphology can be controlled by varying the electrolyte concentration and the electrochemical potential. However, the tear strength of the HAp coating produced by electrochemical deposition is much lower compared to the coating obtained by plasma spraying [27].

In this method aqueous electrolyte containing Ca^{+2} and $(PO_4)^{-3}$ is used, which upon decomposition forms the calcium phosphate crystals and can be deposited on the electrode. The obtained coating is heat-treated in steam at 125 °C for four hours and then calcined under vacuum at 425 °C for six hours to densify the film and improve its bonding to the substrate, the coating is formed gradually through the nucleation and growth process [22][27].

1.3.6 Biomimetic deposition

Biomimetic deposition mimics the mineralization process of bone whereby a biologically active bone-like apatite layer is formed on a substrate surface by immersion in a Hank's balanced salt solution or supersaturated aqueous solutions with ionic composition similar to human plasma at 37 °C for several days to co-precipitate biologically active molecules with apatite crystals onto the substrate. Prior to the deposition process, the substrate material (i.e. Titanium) is ground and polished with silicon carbide (SiC) paper, followed by ultrasonic cleaning and drying. this calcium phosphate coating has an amorphous or amorphous-crystalline structure, with a preferred (00l) crystallographic orientation [22][28].

1.3.7 Sputtering

There are several sputtering techniques, some of them are: diode sputtering, direct current (DC) sputtering, radiofrequency (RF) sputtering, ion-beam sputtering and Magnetron Sputtering, which can be DC or RF. This magnetron sputtering provides high rate deposition compared to the above mentioned techniques [22].

In the sputtering process, a target (or cathode) plate, which has the composition of the coating required, is bombarded by high energy ions generated in a discharge plasma (ionized state of matter). The plasma usually is ionized gas from Ar, N_2 or O_2, situated in front of the target. Due to the voltage between the cathode and the anode the plasma ions are accelerated to the target surface with high energy generating a collision cascade which

involves transfer of energy from the plasma ions to surface atoms of the target, and the atoms of the surface acquire enough energy to leave the target (momentum transfer), this atoms then condense on a substrate as a thin film [29] [30]. As a result of the ion bombardment, secondary electrons are also emitted from the target surface which help to maintain the plasma [30]. This whole process takes place inside a vacuum chamber [29].

In a process of sputtering the thickness of the deposited film depends on the discharge power and the deposition time. When the discharge power is increased the energy of the ions in the plasma increases, this causes a high erosive effect on the target therefore the film is formed in less time [31].

1.3.7.1 Radio frequency sputtering

The main difference between DC sputtering and RF sputtering is the power source used DC or AC respectively (see Figure 4) [32].

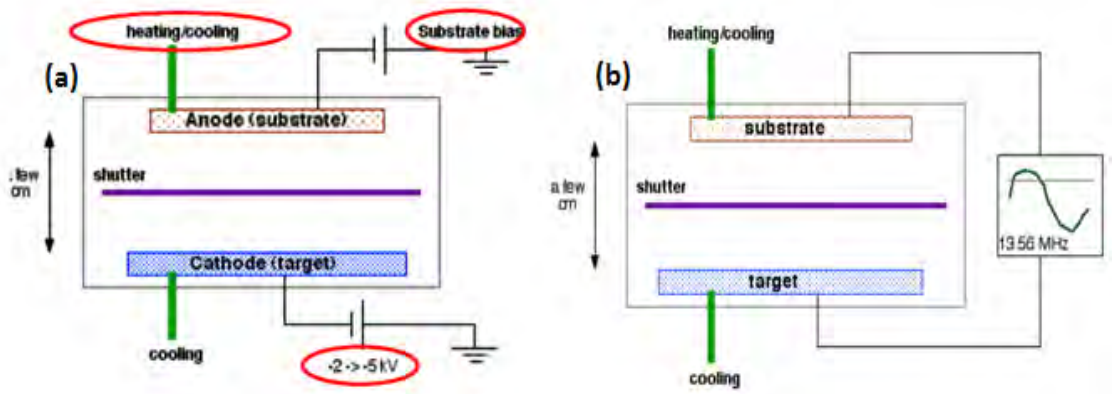

Figure 4: (a) Direct current sputtering system (b) Radio frequency sputtering system [32]

RF sputtering uses radio waves instead of a direct electron current therefore it has different requirements and effects on the sputtering system. The use of DC requires electrically conductive electrodes. If one or both of the electrodes are non-conductive, it can cause a charge build-up on the target material as a side effect due the large number of ions in the chamber. The use of an alternative current AC power source can alleviate this problem because positive charges accumulated during one half-cycle can be neutralized by electron bombardment during the next cycle. However RF systems can present overheating due to the high power required for the process. For example to achieve the same rate of sputter deposition while DC sputtering require between 2,000 and 5,000 volts, in RF sputtering upwards of 10^{12} volts is required for the same electron current [32]. Also the plasma in an RF system can be maintained at lower pressure (15 mTorr), compared to the pressure required for DC sputtering (100 mTorr).

The combination of the method of the radio waves and the lower pressure, makes RF sputtering ideal for target materials which are non-conductive like hydroxyapatite [32].

1.3.7.2 RF Magnetron sputtering (RFMS)

In this technique magnets are placed behind the sputtering target to generate a magnetic

field perpendicular to the electric field (Figure 5). The magnetic field influences the trajectories of moving charged particles producing a confinement of electrons near the surface of the target which increase the probability of electrons striking in the working gas. Also increases the length of the electron path, thereby improving the ionization efficiency. Ion trajectories are not affected significantly by the magnetic field because the relation charge/mass is too small [32] [30].

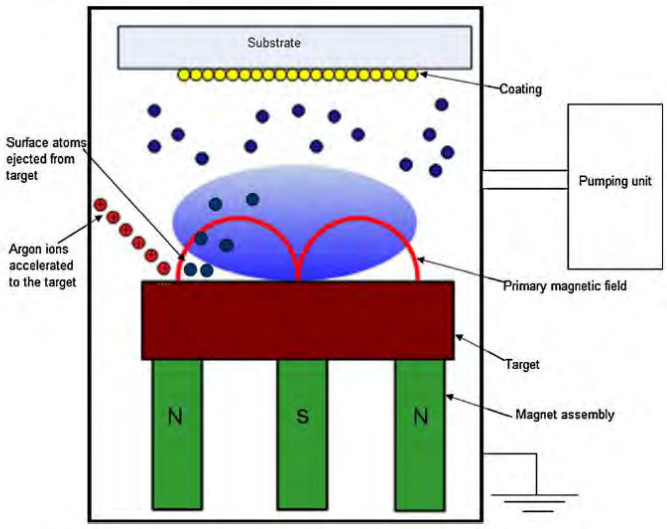

Figure 5: Schematic diagram of the typical RF magnetron sputtering facility with Ar+ plasma [33]

Magnetron sputtering is a promising method for forming a biocompatible ceramic coating onto a metal or plastic substrate [22]. As a result of the efficiency of the ionization of the working gas this method, it presents the following advantages: high deposition rate compared with RF or DC sputtering, lower voltage (normally 500 V, compared to 2 – 3 kV) is required to generate the plasma. Lower pressures (10^{-3} mbar normally, compared to 10^{-2} mbar), reduce the heat of substrate due electron bombardment and reduce the contamination on the film because the high deposition rates which limits the exposure time of the growing film to the vacuum ambient [22] [32][30]. One disadvantage of this process is the target erosion, which does not occur uniformly because the magnetic field causes sputtering to be more intense in places where the magnetic field lines are parallel to the cathode surface (target). The erosion profile of the target takes a particular V-shape, as is shown in Figure 6 [34].

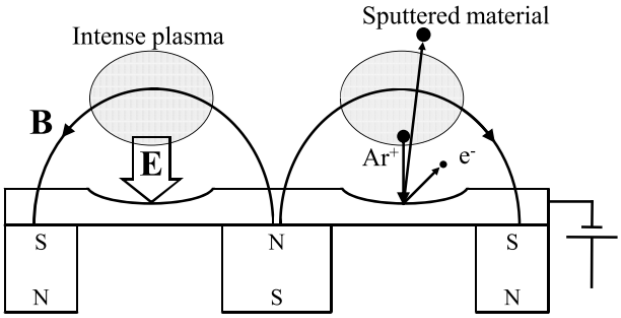

Figure 6: Erosion profile of a Target by magnetron sputtering [34]

Where the electrons are trapped, gas will be ionized then it will sputter the target material. Below this intense plasma, the target erosion will be prominent.

Radiofrequency (RF) magnetron sputtering was used to deposit thin films of HAp on Ti substrate with a deposition rate of 1.0–1.5 mm/h and a film thickness of 0.5–10 mm. X-ray diffraction demonstrated that the sputtered layer was amorphous or crystalline with a preferred (001) crystallographic orientation with the C axis perpendicular to the substrate surface. Scanning electron microscopy showed that the deposited films had a uniform and dense structure. The Ca/P ratio varied between 1.5 and 2.6. [22]

1.3.7.3 Ion beam sputter deposition (IBS)

Ion beam sputtering uses an ion source which consists of a cathode and anode with a common central axis. When a high voltage field of 2-10 kV is applied to the anode an electrostatic field inside the ion source is created, confining electrons around a point in the center of the source. The plasma is produced inside the ion source when the gas flow is injected where the high electric field causes the gas to ionize. The ions are accelerated from the anode region to the exit aperture (cathode) producing in this way a collimated ion beam which is focused on a target to be sputtered [32]. Most applications also use a second ion source (ion assist source) as is shown in Figure 7, which is focused at the substrate to improve the stability and density of the films due to the reactive ions at the surface of the growing film [35].

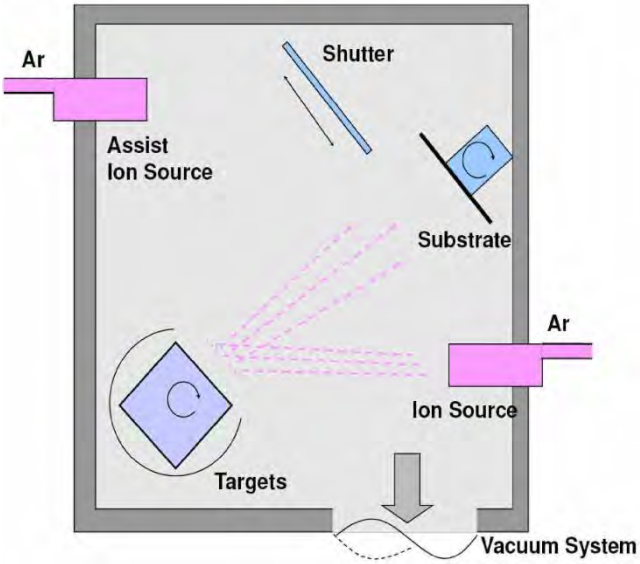

Figure 7: Schematic diagram of the typical ion beam sputter deposition equipment [35].

1.3.8 Pulsed laser deposition (PLD)

The pulsed laser deposition process involves the sputtering of a target using a focused pulsed laser beam. The interaction between laser and target produces a plasma cloud, which is composed of electrons, atoms, ions, molecules, molecular clusters, in vacuum or in a gaseous environment. The material ejected from the target is deposited on a heated substrate (350–800 °C) producing a film [22].

To prepare biocompatible CaP thin films by PLD a UV KrF excimer laser (λ=248 nm) or ArF excimer laser (λ=193 nm) is commonly used. The interaction of the laser with hydroxyapatite target produces the decomposition of hydroxyapatite as $Ca_4P_2O_9$, $Ca_3(PO_4)_2$, CaO, P_2O_5, and H_2O in tha plasma cloud. The substrate temperature during thin films deposition by PLD is typically in the range of 350–600 °C, thus make possible the formation of a highly crystalline with a preferred (001) crystallographic orientation and phase pure coating on implant materials [36].

1.4 Polymethyl Methacrylate (PMMA)

PMMA is an amorphous thermoplastic polymer with chemical formula ($[-CH_2-C[CH_3][CO_2CH_3]-]_n$) and structure as shown in Figure 8. This polymer is biocompatible and non-degradable. It was approved by FDA (Food and Drug Administration) to be used to fabricate reconstructive structures, such as dental implants, craniofacial implants, or as bone cement to remodel lost bone [2].

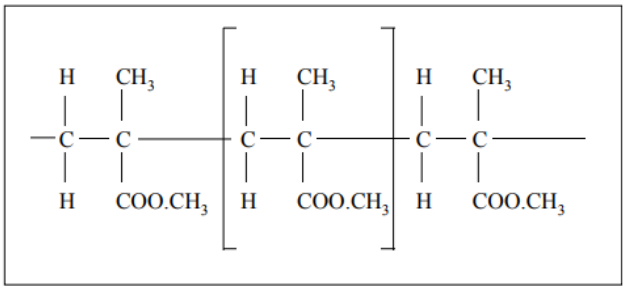

Figure 8: Structure of polymethyl methacrylate[37]

The advantages of PMMA over titanium to be used as a material for craniofacial implants is that it is easier to obtain complex shapes that are required for this type of implants through simple manufacturing processes such as thermoforming, injection, and rapid prototyping with very good aesthetic results [1][2].

1.4.1 Properties of PMMA

PMMA is a transparent (80 – 93%) and colorless thermoplastic. It is hard and stiff, however its resistance to temperature and fatigue are poor as shown in the tables 4 and 5, with low coefficients of thermal-expansion($\sim 5\times10^{-5}$ per K) and pressure-shrinkage ($\sim 5\times10^{-11}Pa^{-1}$)[38].

Table 4: Mechanical Properties of PMMA [38]

Mechanical Properties	Value
Hardness, Rockwell (Scale M)	63.97 M
Microhardness (load 500 mN)	177 MPa
Tensile Strength, Ultimate	47 - 79 MPa
Compressive Strength	188 MPa [39]
Elongation at Break	1 - 30%
Tensile Modulus	2.2 – 3.8 GPa
Flexural Modulus	3 -3.5 GPa
Izod Impact, Notched *	1.2 -20KJ/m^2
Izod Impact, Unnotched*	11 KJ/m^2

* Izod Impact is a single point test that measures a materials resistance to impact from a swinging pendulum. It is defined as the kinetic energy needed to initiate fracture and continue the fracture until the specimen is broken. When it is notched, means that the sample has a notch in the middle.

Table 5: Thermal properties of PMMA

Thermal Properties	Value
CTE, linear 20 °C	60 -130 um/m.K
CTE, linear 20 °C Transverse to Flow	70 - 90 um/m.K
Specific Heat Capacity	1.46 -1.47 J/g.K
Thermal Conductivity	0.19 -0.24 w/m.K
Melting Point	130 °C
ignition temperature	460 °C
Vicat Softening Point - A *	116 °C
Glass Temperature	100 – 105 °C

* Vicat Softening Point is the temperature at which the specimen is penetrated to a depth of 1 mm by a flat-ended needle with a 1 mm^2 circular or square cross-section. For the vicat A test, a load of 10 N is used. For the vicat B test, the load is 50 N.

Compressive strengths for bone cements of PMMA, after to be molded, are of 85-100MPa with a porosity range between 5-35 percent while compressive strengths for cortical bone, which has a range of porosity between 5-10 percent, varies from 130 to 180MPa and for trabecular bone is from 3 to 15MPa with a range of porosity between 70 to 90 percent [2].

Due to the properties mentioned above, PMMA is an alternative to be used as a bone substitute or in craniofacial implants if mechanical strength and porosity can be controlled during fabrication due to its thermoplastic properties the manufacturing of PMMA by 3D printing is possible [2][40].

1.5 3D Printing

The conception of 3D printing is also referred to as rapid prototyping (RP), computer assisted manufacturing (CAM), additive manufacturing (AM), or solid-freeform technology (SFF) [6]. Development of 3D Printing and computer assisted design (CAD) can be used in the manufacture of custom implants due to the improved visualization tools which facilitate the modeling of an implant, and fast and exact manufacture that offers the method of 3d printing. As a result of its advantages this technology has opened up a new horizon for the next generation of craniofacial implants [41].

3D printing is an additive manufacturing process which uses computer assisted design (CAD) software to produces a three dimensional component in a very short period of time [41][40]. The original design is drafted in a CAD program, where it is then converted to a .STL (Standard Tessellation Language or STereo- Lithography) file, which has been accepted as standard for data transfer between the CAD software and a 3D printer [6]. The components can be produced by metal, ceramic and glass deposition or plastic process. The materials are added layer by layer, allowing also the combination of different materials [41][40].

In the last decade, greater importance has been given to the 3D printing technology in the manufacture of bone implants or scaffolds for bone tissue using materials such as, titanium, polymethylmethacrylate (PMMA), bioceramics as hydroxyapatite (HA), polyethylene, and others biodegradable polymers [41]. Polymers such as PMMA or PLA were processed by molten deposition (MDF) and bioceramic or bioglass materials by stereolithography (SLA) [2][41][42].

HAp scaffolds for bone tissue were designed in CAD and manufactured using 3D printing technology. For the manufacture a layer of HAp-powder was deposited on the building platform then this was covered by a binder, water soluble polymer blend (Schelofix), to bond the powder in selected areas and generate the required form, then a new ceramic powder is deposited on the former layer. In this way the process is repeated until obtaining the complete scaffold. Finally air flow air is used to remove unbound powder and the scaffolds were sintered for 2 h at 1300 °C to achieve sufficient strength and remove the organic binder compound [42]. This technique was also applied to obtain craniofacial implants [43].

G. Staffa et. al followed for two years with periodic visits and CT scans, sixty patients treated surgically with a customized porous-HAp implants for large cranial defects. Then G. Staffa et. al concluded that HAp implants can achieve favorable clinical results in cranial reconstruction due to the low adverse reaction and morbidity rates. However this method is a procedure with high costs and a careful selection of the defects to be treated. Although after two years of follow-up mechanical complications have not been reported longer follow-up is necessary to confirm the high safety profile and good performance in cranial defect reconstruction [43].

1.6 3D printing methods

1.6.1 Stereolithography (SLA)

Stereolithography is based on the principle of photo-polymerization to build up components in three dimensions. Acrylic or epoxy resins and ABS are used as raw materials. SLA software cuts the model of the component in a STL file in several layers of printing with a fixed thickness [40].

In SLA the component is printed on a horizontal platform, submerged in a photosensitive liquid resin (monomer). The photo-polymerization of the monomer is caused by ultraviolet light laser (Figure 9). The laser beam travels through the liquid resin surface depending on the numerical 3D model transmitted to the printer. When a layer of material is solidified, the platform descends according to the thickness of the next layer and a new section is treated. In this way the cycles are repeated until the complete volume of the component is obtained. Subsequently the component is post-cured in an ultra violet oven, and finally it is cleaned with a solvent [40][6].

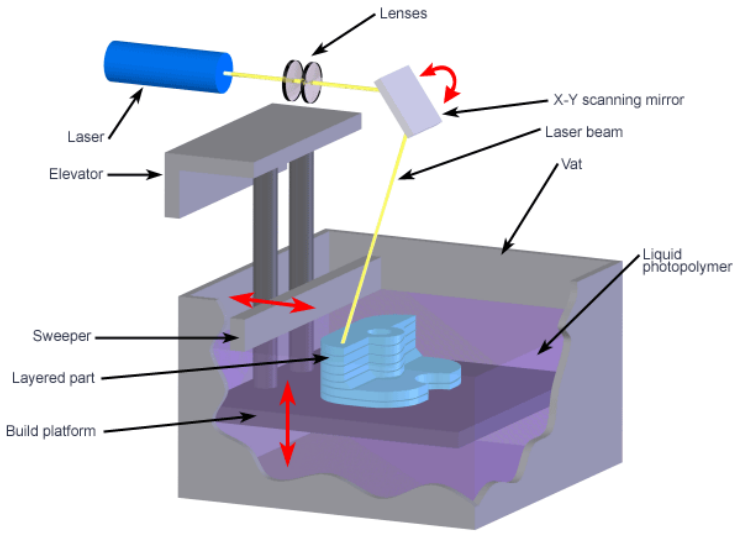

Figure 9: Schematic representation of the printing process by Stereolithography [6]

1.6.2 Selective Laser Sintering (SLS)

To generate a component in three dimensions SLS uses a high power laser, to sinter polymer, metal or ceramic powders. To start the process, the platform is heated to a temperature just below the powder's melting point by infrared heating. This reduces the thermal distortion and facilitates the fusion to the previous layers [40]. A first layer of powder is distributed evenly onto the bed by a roller then a laser beam is selectively scanned over the powder to raise the local temperature to the powder's melting point to fuse powder particles. After the first layer is completed, a second layer of powder is added, leveled, and sintered ageing by the laser in the desired areas. These steps are repeated to create a 3D model. One advantage of this process is the support structures are not required because the powders that are not sintered by the laser serve as support structure. This powder can be removed after fabrication and it also can be recycled. Figure 10 shows a schematic of the process of SLS [40] [6].

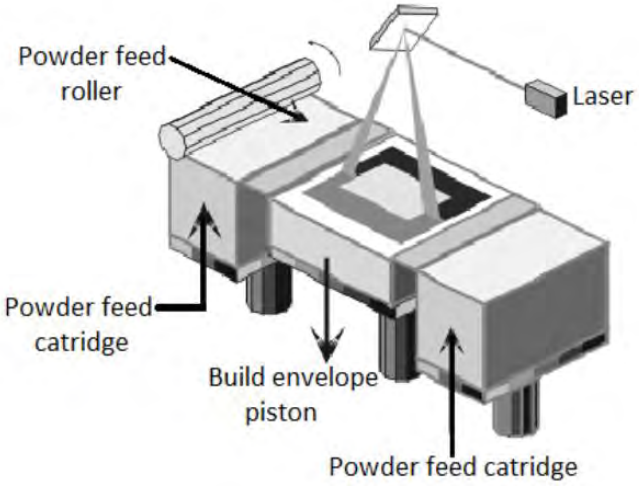

Figure 10: Schematic representation of the printing process by selective laser sintering [40]

1.6.3 Fused Deposition Modeling (FDM)

Developed by Scott Crump in 1980 in the late 80's and marketed in 1990 by Stratasys (USA) company of which Crump was founder [6]. This method is based on the extrusion of a thermoplastic material and the deposition of the extruded material layer by layer on a Jaiganesh movable platform. As is showed in fig. the material is supplied by plastic filament, which is moved by two rollers down to the nozzle tip of the extruder of a print head, where they are heated by temperature control units slightly above its melting temperature. The movable nozzle which has only X-Y movement deposits a molten polymeric material on to the platform in the desired areas layer by layer until obtaining a 3D structure [40].

Components produced by this process have a surface with defects including staircase and chordal effects resulting from the nature of the slicing software and .STL file format, which cuts the piece in several layers. Internal defects can result from heterogeneities in the filament feed diameter and density, as these can affect how the material is extruded from the printer nozzle [6]. A notable advantage of FDM is that it can create objects fabricated from multiple material types by printing and subsequently changing the print material, which enables more user control over device fabrication for experimental use. Besides conventional materials such as PC, polystyrene (PS), and ABS, FDM can also print 3D models out of glass reinforced polymers, binder is typically mixed with ceramic or metal powders, enabling the material to be used in a filament form [6].

In this method, a plastic filament is directed into a heating block where it is heated to a semimolten state (see schematics in Figure 11). The molten material can be printed onto an adjustable stage to form a layer of the desired object. The stage is adjusted (lowered) and another semimolten layer is printed.

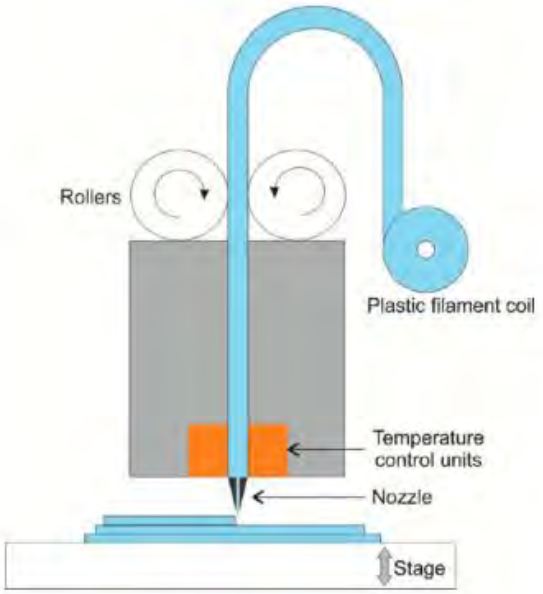

Figure 11: Schematic of an FDM 3D printer [6]

The parameters that can be controlled in the FDM process are the following:

• Extrusion temperature is the temperature of the nozzle, where the material passes through and is molten. This temperature should be higher than the melting temperature of the material due to the high extrusion rates of the printer [40] [44].

• Temperature of the base on which the first layers of material will be deposited to form PMMA substrates, This reduces the thermal distortion and facilitates the fusion to the previous layers [40].

• The directions of impression is referred to the movements of the nozzle to construct the object [44], as is showed in Figure 12.

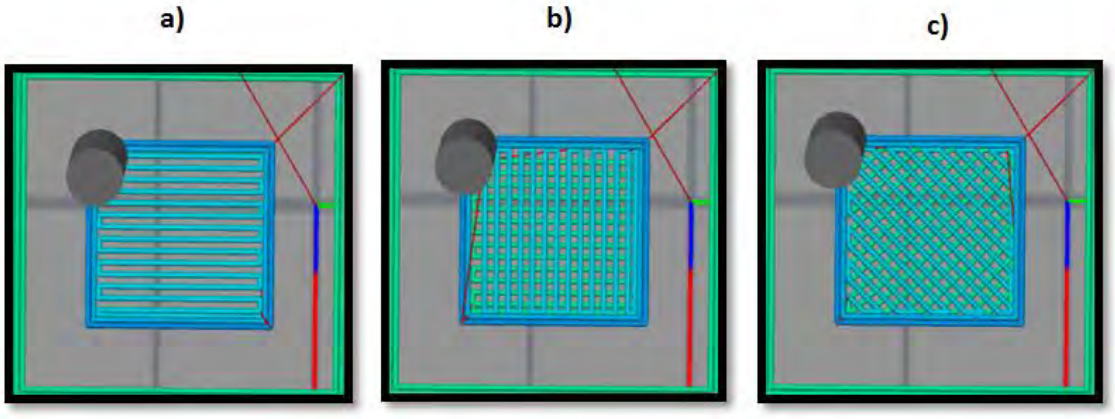

Figure 12: Preview of simplify 3d software for printing objects with different directions a) 90º;-90º, b) 90º; 180º and c)45º; -45º

• Infill percentage is the material quantity that will be deposited inside the object to be constructed, the objects can be from 0% to 100 % (see Figure 13).

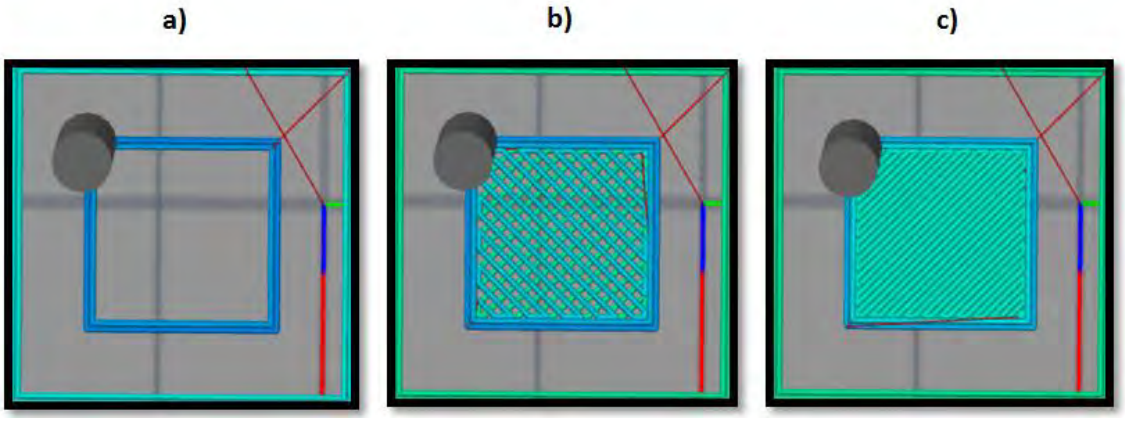

Figure 13: Preview of simplify 3d software for printing objects with different infill a) 0%, b) 50% and c) 100%.

• Layer thickness, is the diameter of the bead which is deposited by the nozzle on the base to form the desired component, therefore each layer forming the fabricated component will have this thickness [44].

As a result of the possible advantages associated with directly manufacturing freeform implants using 3D printing technology, D. Espalin et al. [2]studied the processing PMMA via FDM for direct use in medical applications and conclude the following: PMMA structures manufacturated by FMD, with a porosity of 70 % - 50%, it presents compressive strength of 7 MPa – 16 MPa respectively and it is compared to the range of trabecular bone, which presents a compressive strength of 3 MPa – 15 MPa with 90 – 70 % porosity . Therefore it is expected that as porosity in the fabricated samples decreases, compressive strengths will approach those of molded PMMA bone cement (85-100 MPa), approaching the properties of the cortical bone (130-180 MPa) [2].

1.7 Characterization techniques

1.7.1 Scanning electron microscopy (SEM)

SEM is a technique used to analyze the surface of a specimen on a microscopic level. It can provide information as topography and morphology of the sample, if the microscope is also equipped with X-ray capabilities, the equipment can generate information about the elemental composition of the structure. A specimen is scanned by a focused beam of high energy electrons in an optical column [45]. The principal components of a SEM are showed in Figure 14.

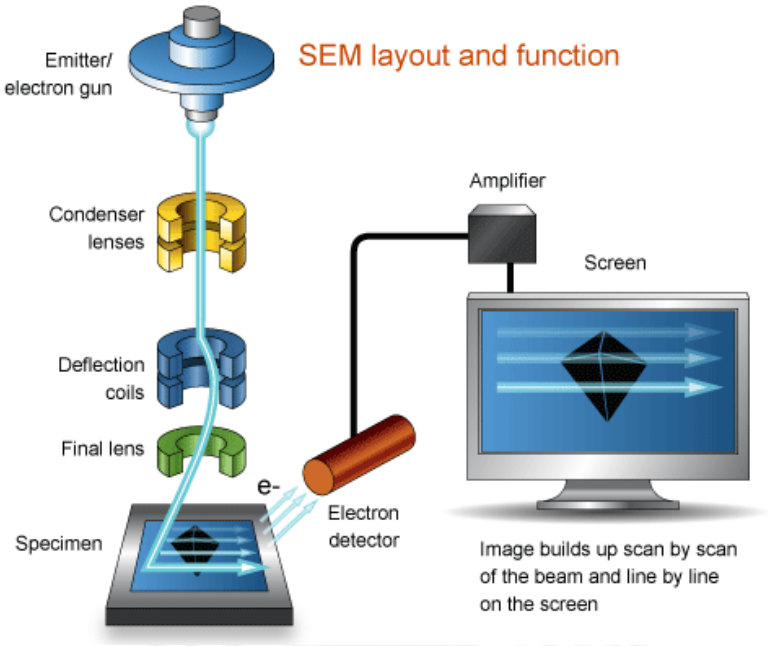

Figure 14: Schematic diagram of the components of SEM [45]

The electron gun uses thermionic emitters where the filament of tungsten or Lanthanum hexaboride (LaB_6) is heated to a temperature between 2000-2700 K by a resistively current to generate thermionic electrons from the tip. These electrons are accelerated to achieve energy in the range 0.1 – 30 keV towards the sample. A series of lenses focus the electron beam on to the sample where it interacts with the sample to a depth of approximately 1 µm.

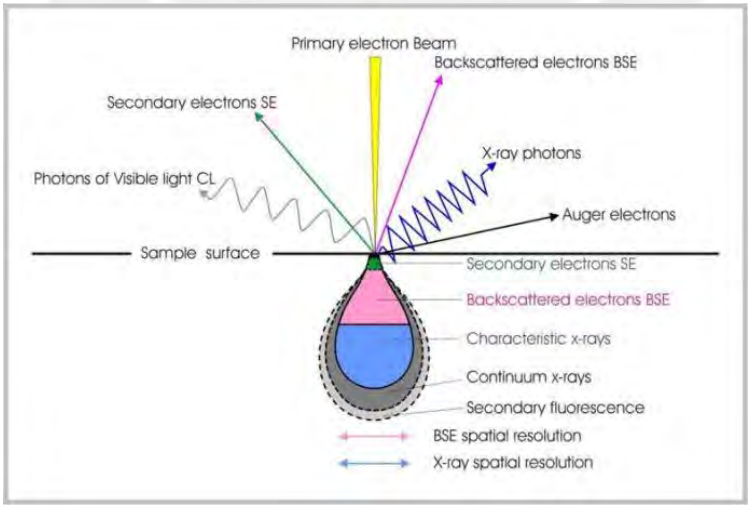

Figure 15: Schematic diagram of electron beam interaction with specimen [46]

As is shown in Figure 15 the electron beam generated (primary electron beam) interacts with the surface of the sample producing secondary electrons (SE), backscattered

electrons (BSE) and Auger electrons. The SE and BSE are captured by the detectors to obtain the sample information.

SE are low energy electrons, typically less than 50 electron volts (eV) which are emitted from the interaction of the primary electron beam with the valence shell of the sample atom, which is hit by the primary, a schematic graphic of the interaction is showed in Figure 16. The SE are used to create a topographic image of a sample [45].

BSE as a definition are primary beam electrons scattered back out of the sample with a range of energy up to the primary electrons (Figure 16). BSE are mainly used to learn about the composition of the sample due to the fraction of BSE (Backscattering coefficient) depends highly on the atomic number of the sample, the greater the backscattering coefficient, the greater the atomic number of the atoms of the sample surface [45].

Characteristic X-ray are generated when the incident electrons knock out the core shell leaving vacancies (holes), this hole is filled by an electron in outer shells to return the atom to its normal state. This transition releases energy in the form of characteristic X-ray (Figure 16).

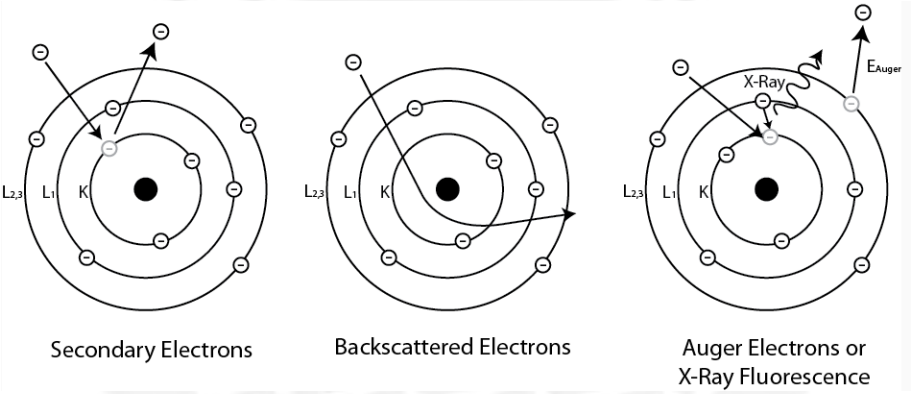

Figure 16: Production of secondary electrons, backscattered electrons, X- Ray fluorescence [45]

Theoretically SEM can achieve 3 nm as a resolution limit imaging while for light microscopy this limit is 200nm. Since the resolution limit is given by Abbe equation (see Eq. 3), the resolution limit (d) deepens on: wavelength of particle (λ), refractive index (n) and semi – angle in radians (α) [45].

Table **6** shows the values of these parameters for light microscope and SEM.

$$d = \frac{0.61\,\lambda}{n sin\alpha} \qquad (3)$$

Table 6: comparison of the resolution limit between light microscope and SEM [45]

Microscopy	λ (nm)	$nsin\alpha$	d (nm)	Magnification
Light	400	1	200	1000
electron	0.3	0.015	0.3	500000

1.7.2 Energy dispersive spectroscopy of X-rays (EDX)

To identify the elements present in a sample EDX analyses the X-rays emitted from a sample during electron irradiation. X-rays are absorbed by the silicon semiconductor detector generating electron–hole pairs. An electric field is used to prevent electron–hole pairs from immediately recombining in order to determine the number of them by measuring the corresponding current pulse in a basic detection cycle.

The formation of one electron–hole pair in a silicon semiconductor requires approximately 3.8 eV of energy. Thus the number of pairs (n_{eh}) formed by the total absorption of the energy (E_{ph}) of one X-ray photon can be expressed by:

$$n_{eh} = \frac{E_{ph}}{3.8\ eV} \qquad (4)$$

In this way every pair generated is counted and then these are summed up und reconstituted in one x-ray count using a multichannel analyzer (MCA). Finally an energy spectrum is obtained which shows how the accumulated x- ray counts of the channels (ordinate) depend on the corresponding photon energy (abscissa), as demonstrated in Figure 17 for the spectrum of calcite [46].

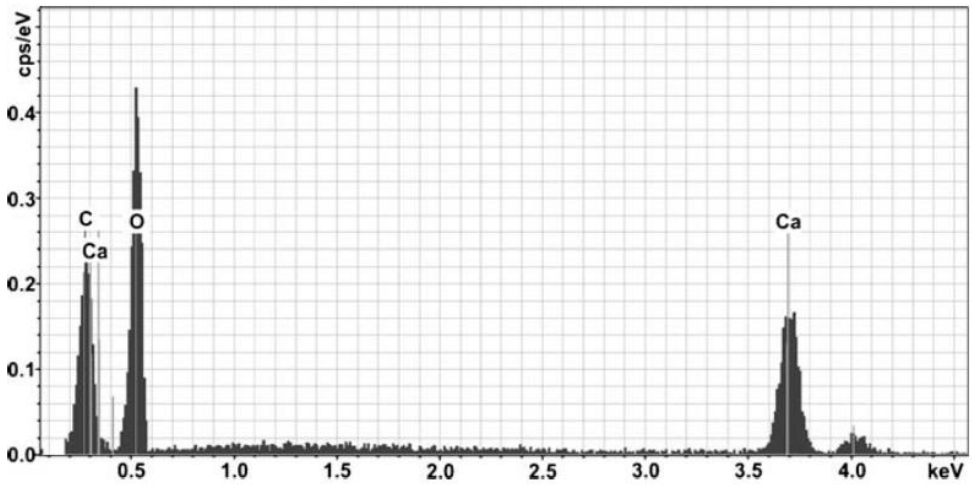

Figure 17: EDX spectrum taken from a small particle (Calcite, CaCO3) [46]

1.7.3 X-Ray diffraction (XRD)

XRD is an analytical technique which uses X-rays to distinguish between amorphous and crystalline materials, it also provides information on crystal structure, phase, preferred crystal orientation (texture), and other structural parameters, such as average grain size, crystallinity, strain, and crystal defects [47] .

The X-rays are produced in a vacuum tube made of a glass or metal, this tube has 2 electrodes, a cathode (tungsten filament) and an anode (tungsten target), which are separated by a distance of about 1–2 cm. These electrodes are connected to a negative (Cathode) and positive (anode) high- voltage cables from the x-ray generator. In an isolated circuit the cathode filament is connected to a low-voltage power source, when this circuit is activated the filament is heated due to its electrical resistance and releases electrons by a process known as thermionic emission. Then a high voltage (50–150 kV) is applied to the circuit which connects anode and cathode, it causes electrons are accelerated to the anode where the interaction between the highly energetic electrons with the anode generates X-ray as was explained before [48]. A scheme of a XRD tube is showed in Figure 18.

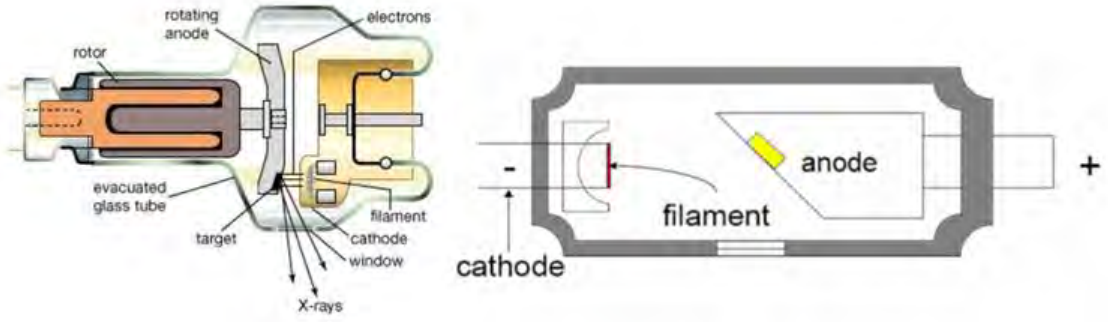

Figure 18: Schema of XRD tube [48]

1.7.3.1 X-ray diffraction analysis

The X-rays are scattered by the electrons of the specimen atoms without a change in wavelength. X-rays scattered are measured in diffraction experiments, to obtain information about the atoms distribution in the sample. When the specimen is a crystalline solid, Bragg's law can be applied to know the crystal structure of the material [49].

In Equation 1 Bragg's law is described**,** where the variable d_{hkl} is interplanar spacing between atomic layers in a crystal, λ is the wavelength of the incident x-ray beam which impinge upon the planes at an angle θ and are deflected at the same angle, planes have Miller index (hkl) [49]. A schema is showed in Figure 19.

$$n\lambda = 2d \qquad (1)$$

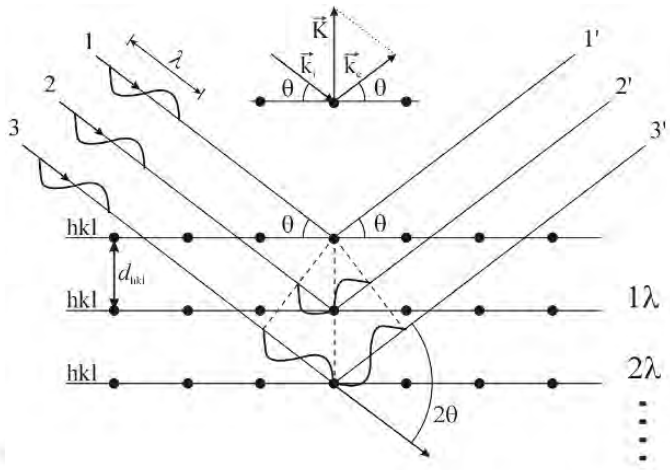

Figure 19: Diffraction from an ordered arrangement of atoms [17]

X-Ray diffractometer

An X-ray diffractometer is an instrument designed for the collection of accurate X-ray diffraction data. Its basic components are: X-ray source, a goniometer where specimen is mounted, and a detector for collecting scattered X-ray photons at a known scattering angle [51]. There are two focusing configurations in the diffractometer: Bragg Brentano and Grazing Incidence. The Bragg-Brentano configuration provides a high penetration depth which allows detecting the atomic layers which are parallel to the substrate surface, while in grazing incidence configuration, the system collects diffraction from lattice planes which are perpendicular to the surface [52].

1.7.4 Micro-hardness

The micro-hardness test is commonly used to estimate the mechanical properties of coatings or thin films. This test uses an indenter probe that is displaced into a surface under a specific load less than 10 N. When the load is higher it is called macro-hardness. The indentation typically has a defined time and to determine hardness depth of indentation is measured [53][54].

Hardness and reduced elastic modulus are calculated commonly using the Oliver and Pharr method [55]. In this method, the hardness is given by:

$$H = \frac{P_{max}}{A_c} \quad (5)$$

Where P_{max} and A_c are denoted as the maximum identation load and the projected contact area, respectively. The reduced elastic modulus (E_r) is given by:

$$E_r = \frac{\sqrt{\pi}}{2}\frac{S}{\sqrt{A_c}} \quad (6)$$

Where S is the contact stiffness. E_r is related to the elastic modulus if considering the elastic modulus of the thin film,E_f, as follows:

$$\frac{1}{E_r} = \frac{1-v_i^2}{E_i} + \frac{1-v_f^2}{E_f} \quad (7)$$

Where E_i is the elastic modulus if the indenter and $v_i$and v_f are Poisson's ratios of the indenter and thin film, respectively [56]. In 2004 W. C. Oliver and G. M. Pharr presented advances in understanding and refinements to methodology for the measurement of hardness and elastic modulus by instrumented indentation [57].

To determine only the mechanical properties in very thin films, hardness and modulus of elasticity, the use of models is suggested that introduces the thickness of the film into the adjustment parameters if it is possible [58].

The ratio of indentation depth to thin film is recommended to be less than 1/10−1/20 of the film thickness, in order to eliminate the influence of the substrate and guarantee its accuracy[58].

Surface Roughness

Surface roughness is defined by two profile parameters : arithmetical mean deviation of the assessed profile (Ra), also known as the center line average (CLA) and maximum height of assessed profile (Rz) [59].

Ra represents the area between the roughness profile and its central line, which is called mean line, or the integral of the absolute value of the roughness profile height over the sampling length[60], (see Figure 20). The integral formula of Ra can be expressed as:

$$Ra = \frac{1}{l}\int_0^l |z(x)|\,dx \quad (8)$$

Where is z(x) is the height profile deviation from the mean line and l is the sampling length [61].

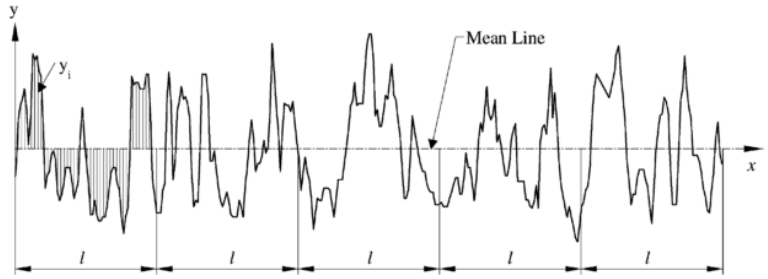

Figure 20: Definition of the arithmetic average height (R_a) [61]

Rz is the average of the summation of the five highest peaks and the five lowest valleys along the assessment length of the profile [61], as is showed in Figure 21. The mathematical definition is the following equation :

$$R_z = \frac{1}{2n}\left(\sum_{i=l}^{n} Pi + \sum_{i=l}^{n} Vi\right) \quad (9)$$

Where *n* is the number of samples along the assessment length.

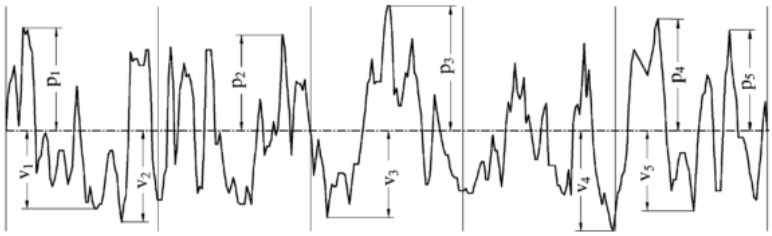

Figure 21: **Definition of the ten-point height parameter (R_z)** [61]

Contact-type surface roughness measurement is performed by using a stylus tip in the perpendicular orientation of the surface of the sample (Figure 22). This stylus tip makes direct contact with the sample while traverses the surface and the vertical motion of the stylus is converted into an electrical signal. The electrical signal go through an amplification and digital conversion process to be recorded [60][62].

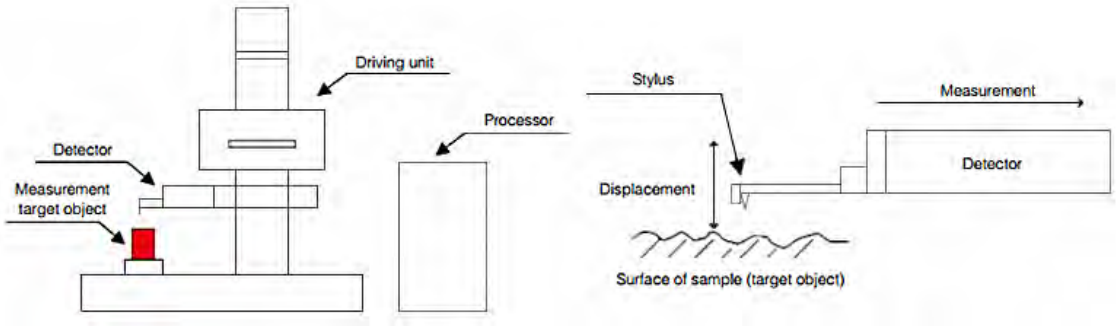

Figure 22: Contact-type surface roughness measuring system [60]

2 Experimental Procedures

In this section, the experimental details of the manufacture of PMMA substrates, HAp target manufacturing, thin films deposition and analytic techniques of the thin films are presented.

2.1 PMMA substrates manufacturing

The substrates were developed using a desktop printer (Makerbot Replicator 2X) by the method of fused deposition modeling (FDM) and a filament of PMMA manufactured by 3D Rigid. To manufacture five different substrates of PMMA with variable infill percentage the following parameters were used:

• The extrusion temperature or the temperature of the nozzle was maintained at 245 °C since melting temperature of PMMA is 160 °C and it ignites at 460 °C. This temperature was used in previous investigations [2] and is in the temperature range recommended by the PMMA filament manufacturer.

• Temperature of the base was the one recommended by the manufacturer of PMMA filament (60 °C).

• The directions of printing were 45° and -45°, since similar thermoplastic materials printed to these directions present a low level of anisotropy [44].

• Different infill percentages were used (100%, 90%, 80%, 70%) to obtain different percentages of porosity in the substrates.

• Layer thickness: The layers forming the PMMA substrate have a thickness of 0.2 mm.

The shape of the substrate with the required dimensions was designed in Simplify 3D software, where the parameters for the printing were entered. The dimensions of the design of the PMMA substrates were (20 mm x 20 mm x 2.5 mm), the dimensions of the printed PMMA substrates were the same with an error range of 0.1-0.4 mm (Figure 23).

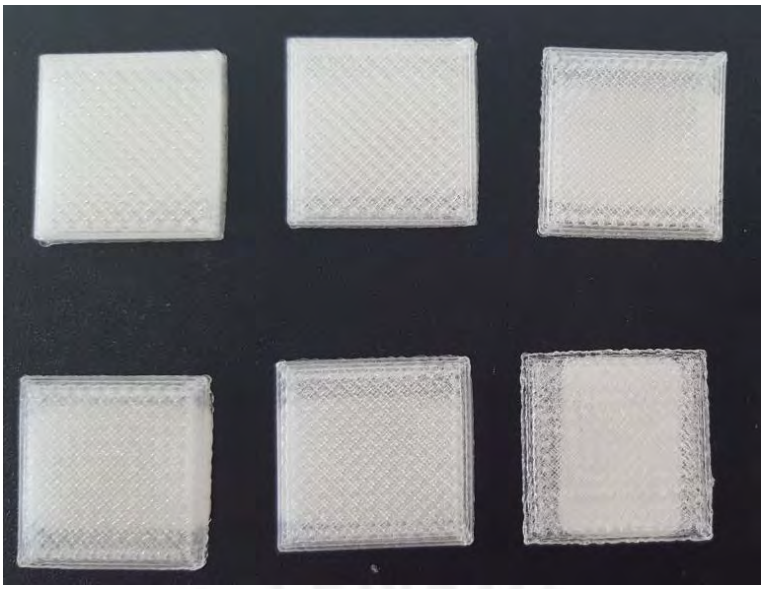

Figure 23: PMMA substrates obtained by 3D-MDF printing with different infill percentages (60%, 70%, 80%, 90%, 100%). The dimensions of the PMMA substrates are 20 mm x 20 mm x 2.5 mm.

2.2 Target manufacturing

The target used for the deposition of HAp films on PMMA substrates by ion beam sputter deposition, was made in coordination with Alfonso Ugarte, who also used the target for the development of his investigation "**Preparation and characterization of sputtered Hydroxyapatite thin films**". The target was selected after a previous study, in which different targets were manufactured with different parameters, these targets were analyzed and the one that presented a better performance was selected.

The target was obtained by the sintering of HAp powders, which were manufactured by Medicoat. These powders have a particle size of -135 + 0.45 μm (Figure 24), with an angular morphology and the pore size is 1.55 ± 0.44 μm (Figure 25, Figure 26)

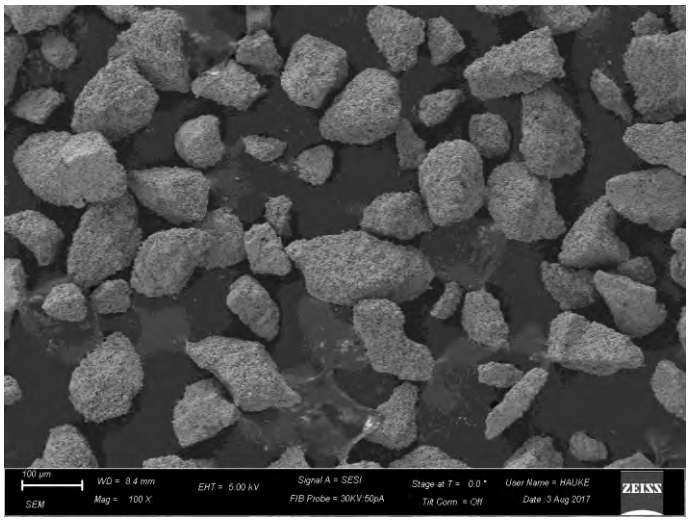

Figure 24: SEM micrographs of the HAp powders (Mag = 100X)

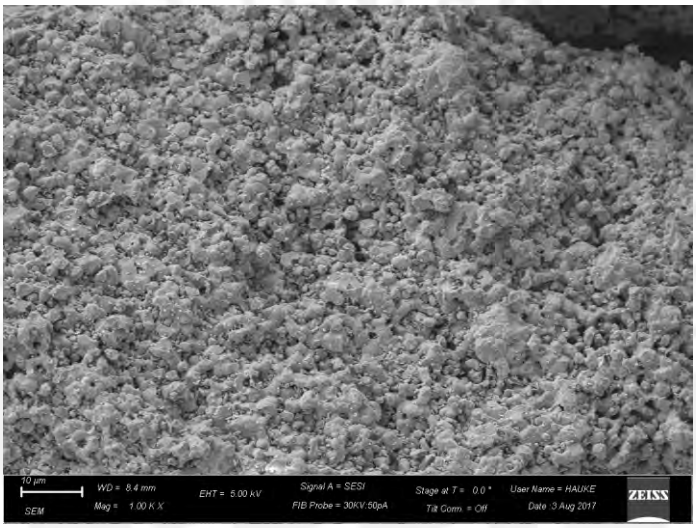

Figure 25: SEM micrographs of the HAp powders where porous structure of the particles is observed (Mag = 1.0 KX)

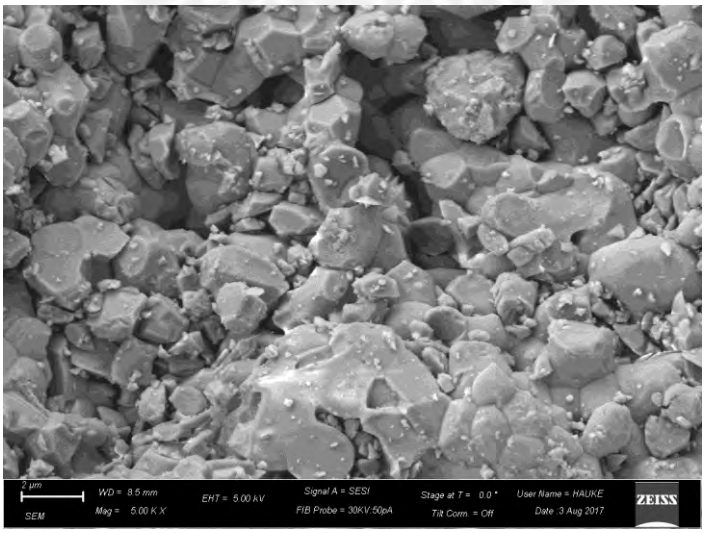

Figure 26: SEM micrographs of the HAp powders showing the pores and grain limit (Mag = 5.0 KX)

The results of the analysis of the HAp powders by EDX are shown in Table 7, and EDX spectra in Figure 27

Table 7: Chemical composition of HAp powders and ratios

Element	Wt%	At%
C	2.99	6.15
O	32.35	50.05
Mg	0.28	0.28
P	20.73	16.56
Ca	43.65	26.96
Ratios	**Theoretical**	**Powder**
Ca/P	1.667	1.628
O/Ca	2.600	1.856
O/P	4.333	3.022

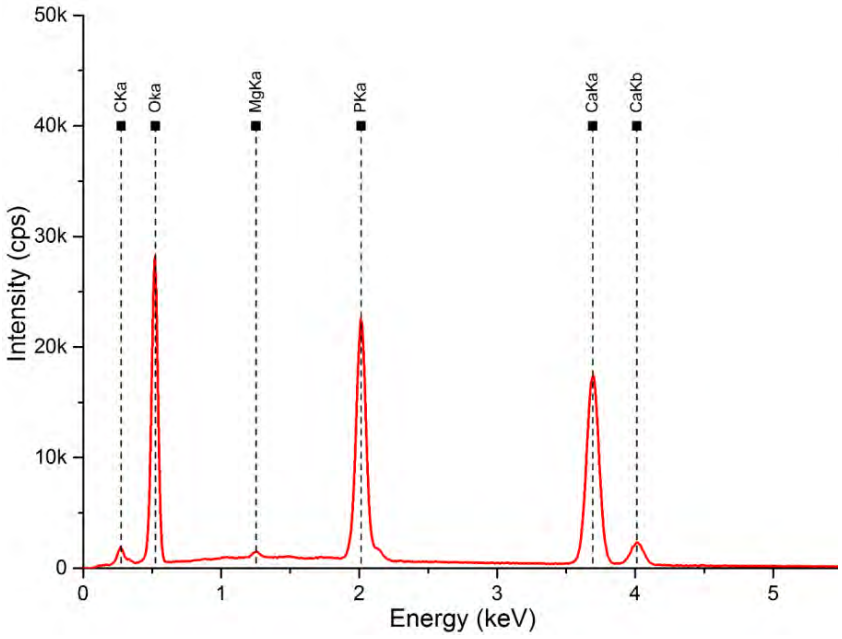

Figure 27: EDX spectra of the HAp powders composed by C, O, Mg, P and Ca.

Targets sintering

The HAp particles were uniaxially compacted in a die, whose internal diameter was 40 mm using compaction equipment Weber-Pressen at different pressures (24 MPa, 40 MPa, 56 MPa, 72 MPa, 80 MPa) and at room temperature in IMN in TU-Ilmenau. Two targets were compacted with an additive system consisting of a binder and a plasticizer. Polyvinyl alcohol (PVA) enhances the cohesive forces between the particles and polietilenglycol (PEG) gives flexibility to the binder [63]. For all other targets only water was added. Targets were sintered at 1473 K using a Nabertherm furnace with temperature control in air atmosphere in Arrheniusbau - TU Ilmenau. The sintering conditions are shown in Table 8.

Table 8: Sintered conditions for the green discs in air atmosphere.

Heating schedule	HAp (g)	Additives	Pressure (MPa)
1	15.0	H_2O (3 %wt)	24
	5.0	H_2O (3 %wt)	24
	3.5	H_2O (3 %wt)	24
2	2.3	H_2O (3 %wt)	40
	2.3	H_2O (3 %wt)	56
	2.3	H_2O (3 %wt)	72
	2.3	H_2O (3 %wt)	80
1	2.3	H_2O (3 %wt)	72
	2.3	PEG (2 %wt) + PVA (1 %wt)	72
2	2.3	H_2O (3 %wt)	72
	2.3	PEG (2 %wt) + PVA (1 %wt)	72

For the sintering of the targets two heating schedules (HS) were used as shown in Figure 28. Where in HS1 the sintering temperature is 1473 K, which was maintained for 2 hours and in HS2 the same temperature was maintained for 4 hours.

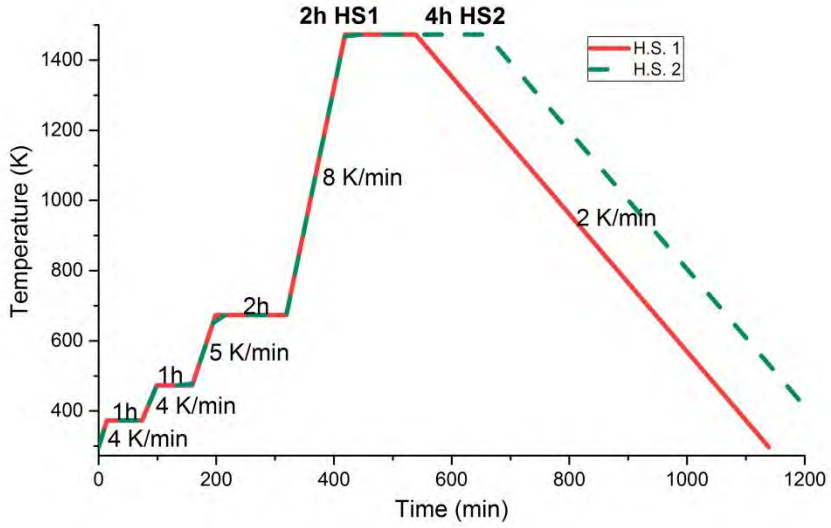

Figure 28: Heating schedule 1 and 2 for sintering process

2.3 Coating deposition

To cover the substrates two techniques of deposition were used, magnetron sputtering and ion beam sputter deposition. For the magnetron sputtering deposition, a target manufactured by Stanford Advanced Materials was used, while for Ion beam sputter deposition the target used was manufactured from HAp microparticles, as indicated in section 3.2.

2.3.1 Magnetron sputtering deposition

The PMMA substrates were cleaned ultrasonically in isopropanol and then dried in nitrogen flow before to be coated with calcium phosphate by RF magnetron sputtering in a vacuum chamber, which is equipped with three flexible magnetrons, target holder, substrate holder, cooling systems, controllers for gas flow and power controllers. This equipment is in the Laboratory of Materials Science of the PUCP- Peru.

The target of Hydroxyapatite provided by Stanford Advanced Materials with 51 mm of diameter was fixed in the vacuum chamber on its respective holder, at 7 cm distance from the target were fixed the PMMA substrates. The background pressure before the deposition process was 1.5×10^{-5} mbar. The working pressure was around to 6.7×10^{-3} mbar in Argon and Oxygen gas flow of 15 and 12 sccm respectively at room temperature (RT). A shutter was used to isolate the PMMA substrates during 15 min to ensure the cleaning and conditioning process of the target. The deposition rate was 0.56 nm/min with a power of 100 W, therefore a coating thickness about 200 nm was obtained after 6 hours of deposition. The deposition conditions for PMMA substrates are summarized in Table 9.

Table 9: Sputtering conditions

Substrates	Target	source	Gas Ar/O2 sccm	P work mbar	Power (W)	Time (min)
PMMA - printed	HAp	RF	15 - 12	$6.7x10^{-3}$	100	360

2.3.2 Ion beam sputter deposition

The PMMA substrates were cleaned ultrasonically in isopropanol and then dried in nitrogen flow before to be coated with calcium phosphate by ion beam sputter deposition using the Precision Etching and Coating System (PECS), Gatan – model 682, in the IMN of the TU-Ilmenau. The target used was manufactured in TU- Ilmenau as detailed above, which was fixed inside the vacuum chamber of the PECS, the PMMA substrates were fixed in the respective holder of this equipment.

The deposition was performed in 10 intervals, each interval with 20 min of deposition and 10 min of cooling, to avoid overheating of the target and the substrate. Therefore the effective deposition time was 200 min. The working pressure was $8x10^{-3}$ Pa and the beam energy was set at 4.6 keV being able to reach the right and left gun in a range of 310 μA –

320 µA, with these parameters a deposition rate of 1.5 nm/min was obtained. The thickness of the film obtained was about 300 nm.

2.4 Characterization techniques

2.4.1 SEM

Scanning electron microscopy images were taken on a Hitachi S 4800 using an acceleration voltage of 5 kV and sample current of approx. 11 µA in order to capture high resolutions images. Different magnifications of 10, 25, 50 and 100 kx were used to to observe the morphology of the films with a suitable resolution.

2.4.2 EDX

EDX spectra were obtained using a SEM Philips XL30 equipped with an EDAX system. All the EDX spectra were accumulated during 100 s with a spot size of 6.4 mm^2, an acceleration voltage of 10 kV and a sample current of around 16 µA. The low acceleration voltage was chosen in order to not penetrate the substrate with the electron beam and, therefore, to avoid the PMMA signal of the substrate.

2.4.3 XRD

The diffraction experiments were performed on a Bruker D5000 theta-theta X-ray diffractometer equipped with a Cu Kα (λ = 1.54060 Å) radiation source and a Goebel mirror. For the HAp target analysis, Bragg-Brentano configuration was performed to get high penetration depth in the sample. X-ray experiments were carried out using a time/step of 2 s, a step-size of 0.03°/step and a diffraction angle (2θ) covering the range from 5 to 70 °. For the films analysis grazing incidence diffraction at 3° was performed to get higher intensity by the detector and avoid the substrate signal. X-ray experiments were carried out using a time/step of 2 s, a step-size of 0.03°/step and a diffraction angles (2θ) covering the range from 5 to 70°.

The identification and analysis of the crystalline structure were done using the EVA software and the PDF file 089-4405.

2.4.4 Microhardness

The hardness experiments were carried out using the Picoindentation HM 500. The indentation tests were performed using as maximum test load: 0.2 mN and a maximum load application time of 20 s. Hardness and reduced elastic modulus were calculated using the Oliver and Pharr method.

2.4.5 Roughness

The roughness measurements were conducted using a contact mode roughness instrument (Alpha – Step IQ) from KLA Tencor, the data analysis was made by the software with the same name.

3 Results and discussions

The following section is divided in two parts. First, the results of the characterization by XRD, SEM, and EDX of the manufactured targets are presented. Second, the results of the characterization of the calcium phosphates coatings on PMMA substrates obtained by magnetron sputtering and ion beam sputter deposition, using XRD, SEM, EDX, microhardness, and roughness measurement, are described.

3.1 Target Analysis

The diffraction peaks from the XRD patterns of the powder and green targets are shown in Figure 29 where the diffraction peaks were identified using the database of EVA - PDF file 089-4405. In this figure HAp 3.5g, 5g and 15g corresponds to the mass of HAp used for the compaction and sintering of the target.

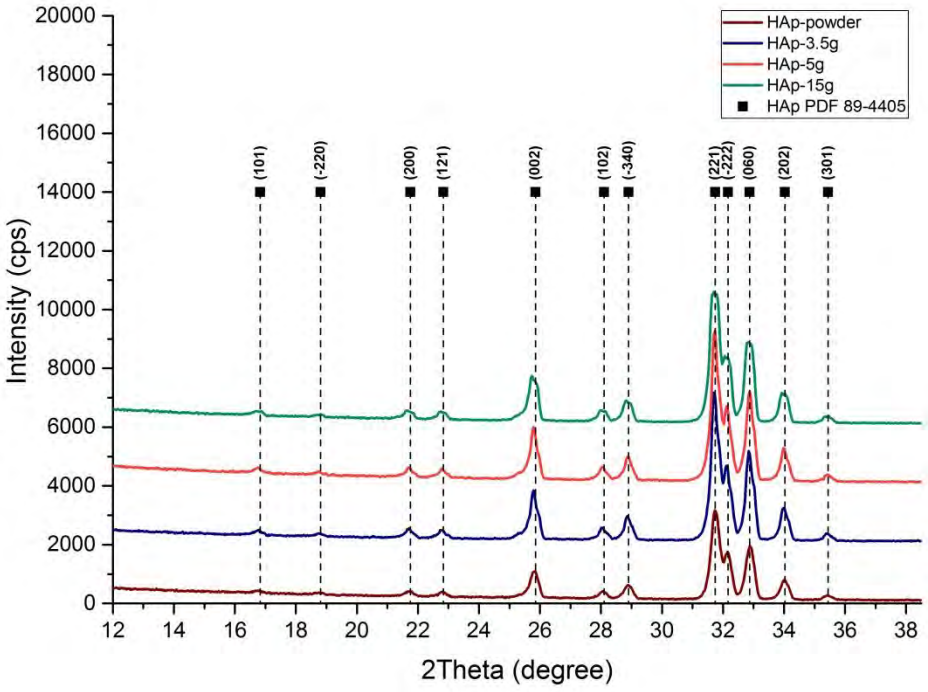

Figure 29: Diffraction peaks from the XRD patterns of the powder and green targets

The powder und green target present the characteristic peaks of monoclinic HAp with the lattice parameters: a = 0.94 (3) nm , b=2a = 1.89 nm and c = 0.69 (3) nm, γ = 120° for HAp monoclinic while for HAp hexagonal a = b= 0.94 nm and c= 069 nm[12][64].

The difference between the monoclinic HAp and the hexagonal HAp is the orientation of the hydroxyl groups. In the hexagonal HAp the OHs are positioned in the columnar arrangements parallel to c-axis of the unit cell, and the adjacent OHs point in opposite directions (two mirror planes at 1/4c and 3/4c) [65]. This configuration implies that there would be interference between adjacent OHs but it is possible by replacement of an OH- with a vacancy, or F^-,Cl^-, the omission of an OH^- can provide reversal points for the O-H direction within within a column [64] [65].

In the monoclinic HAp, all of the OHs in a given column are pointed in the same direction, and the direction reverses in the next column.
HAp sufficiently free of impurities (F-,Cl-) and vacancies might also exhibit intercolumn ordering resulting the monoclinic structure of the P21/b space group [64]. Therefore, the monoclinic form of HAp is the most ordered and the thermodynamically most stable form, even at room temperature [65].

In Figure 30 the diffraction peaks from the XRD patterns of the sintered targets are shown where 2.3 g HAp were previously compacted at different pressures 40; 56; 72; 80 Mpa. The sintering was carried out following the HS2 (heating schedule 2, as defined in the previous chapter) at 1200 °C for 4 hours.

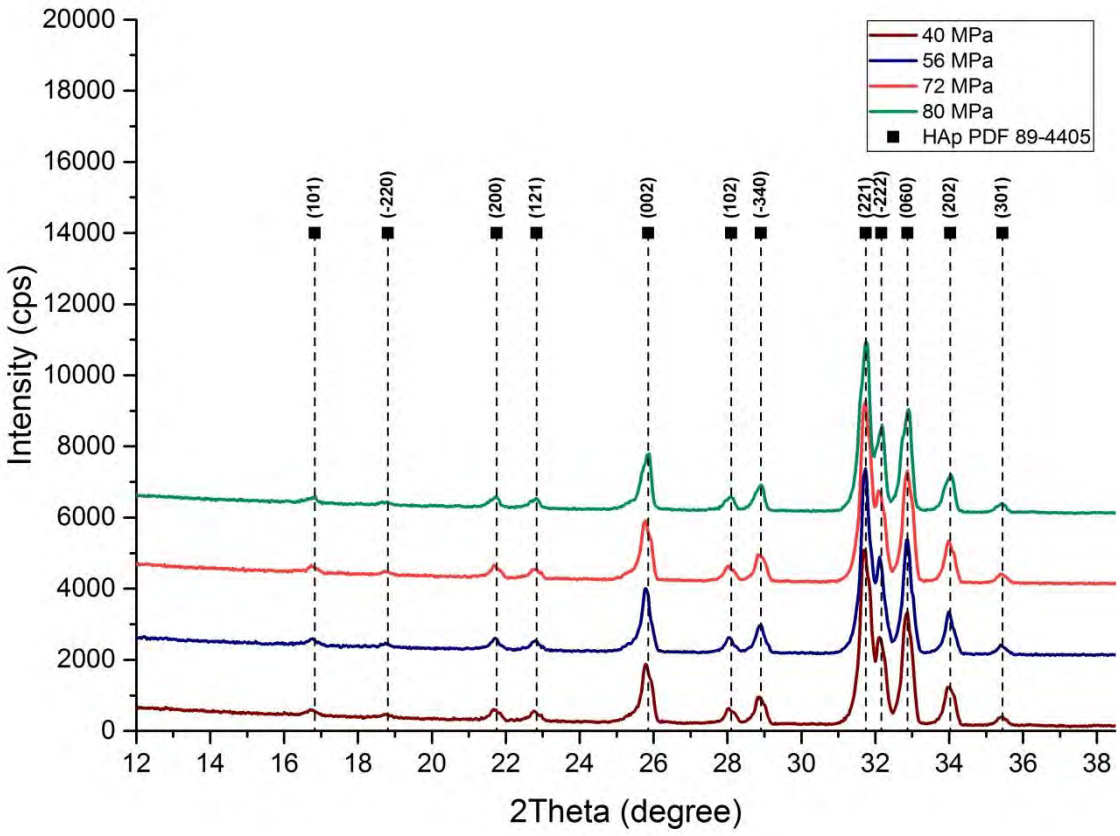

Figure 30: Diffraction peaks from the XRD patterns of the sintered targets, previously compacted at 40; 56; 72 and 80 Mpa

The graph (Figure 30) shows that after compacting and sintering, the targets still exhibit the characteristic structure of monoclinic HAp. If these XRD patterns are compared to the XRD patterns from the HAp powder they are very similar and do not show significant changes.

Table 10 shows the values of density of the green targets, the variation of the density after the sintering and the percentage (**ρ (%)**) in relation to the theoretical density of the hydroxyapatite (3.14 g/cm^3). Table 11 shows the linear shrinkage values.

Table 10: Density behavior for HAp discs fabricated with 40; 56; 72 and 80 MPa at 1200 °C (4h / H_2O).

Pressure (MPa)	Green density (g/cm^3)	Sintered density (g/cm^3)	Theoretically density – Eq. 9 (g/cm^3)	Variation (%)	ρ (%)
40	1.29	1.64	2.61	27	52
56	1.31	1.68	2.66	28	53
72	1.33	1.69	2.6	27	54
80	1.34	1.73	2.61	29	55

Table 11: Thickness variation or shrinkage for targets with 40, 56, 72 and 80 MPa at 1200 °C (4h / H_2O).

Pressure (MPa)	Green thickness (mm)	Sintered thickness (mm)	shrinkage (%)
40	1.42	1.12	21.5
56	1.40	1.10	21.2
72	1.38	1.10	20.3
80	1.37	1.09	20.0

The results shows that an increase in the compaction pressure resulted in an increase in the initial relative density of the green target (green density) and in the density after sintering. Linear shrinkage decreases with the increase of the green density. This agrees with the literature, where, green density (f_G), density after sintering (f) and linear shrinkage ($\frac{\Delta L}{L_0}$) can be related with the following equation [14]:

$$f = \frac{f_g}{(1 - \frac{\Delta L}{L_0})^3} \quad (10)$$

When the equation 10 is applied, the theoretical (f) is higher than the real density as is showed in Table 11**.** This can be explained as **Eq. 10** is considered to apply in an ideal case, where the mass is conserved, where an isotropic shrinkage occurs; also, the binder and plasticizers masses are ignored in calculating the green density [66]. In the present work, binder and plasticizers were used, which burn out in sintering. In addition, the mass is not conserved during sintering, since HAp lost the adsorbed water in the range of 25 to 200 °C, then lost the lattice water between 200 and 400 °C, and also lost OH ions at temperatures about 900 °C [18], as was explained in **secc. 2.2.2**. Therefore, the low density after the sintering can be attributed to the loss of mass during the sintering. Both

cases, real (from this investigation) and ideal, follow the same trend, the greater the green density the lower the shrinkage, as shown in Figure 31.

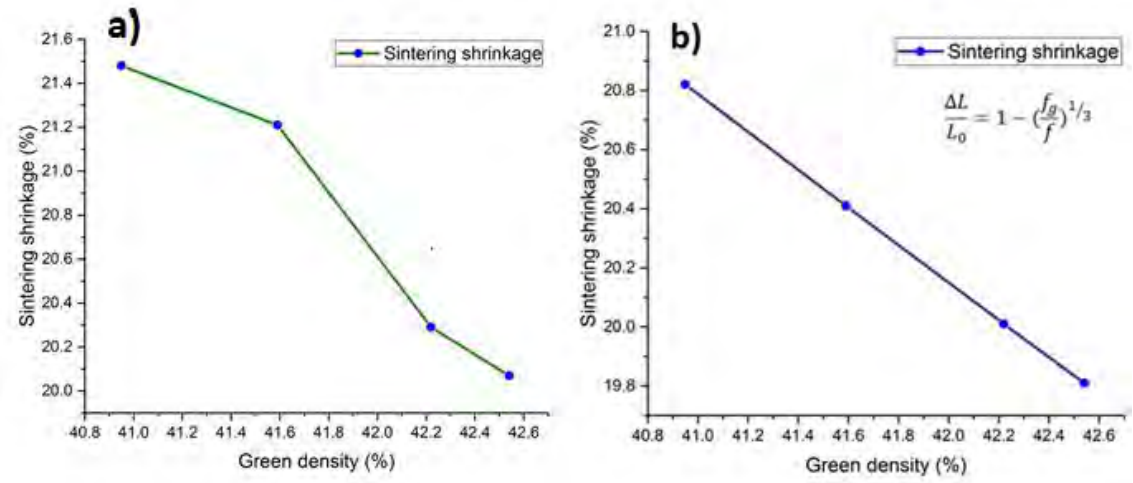

Figure 31: a) Real case: Relation between sintering shrinkage and green density for HAp sintering, with sintered density in the range 1.64-1.73 g/cm^3 (52.0%-54.9%) ; b)Ideal case: Relation between sintering shrinkage, green density, and sintered density given by equation 10 illustrated for final densities of 2.6 g/cm^3 (84.5%)

According to these results, the target with higher density and lower linear shrinkage is the target compacted at 80 MPa**.** However, the target, which was compacted with a pressure of 80 MPa exhibited crack-like defects that were generated during the ejection of the target from the die due to radial and shear stresses, which are generated on the green targets when a uniaxial pressure is applied on the powders. Furthermore, the particles are subjected to elastic compression, contributing to the formation of these defects [67]. Therefore, the pressure selected for the compaction of the targets was 72 MPa.

Figure 32 shows the diffraction peaks for the XRD patterns of the targets, which were compacted at 72 MPa, and then sintered at 1200 °C. The conditions that were varied are: maintenance time in the oven (2 and 4 hours) and additives (H_20 and PVA+PEG), which define the identification of the sample (i.e. Hap-2h-H2O corresponds to the HAp target obtained using H2O as additive and sintered for 2 h)

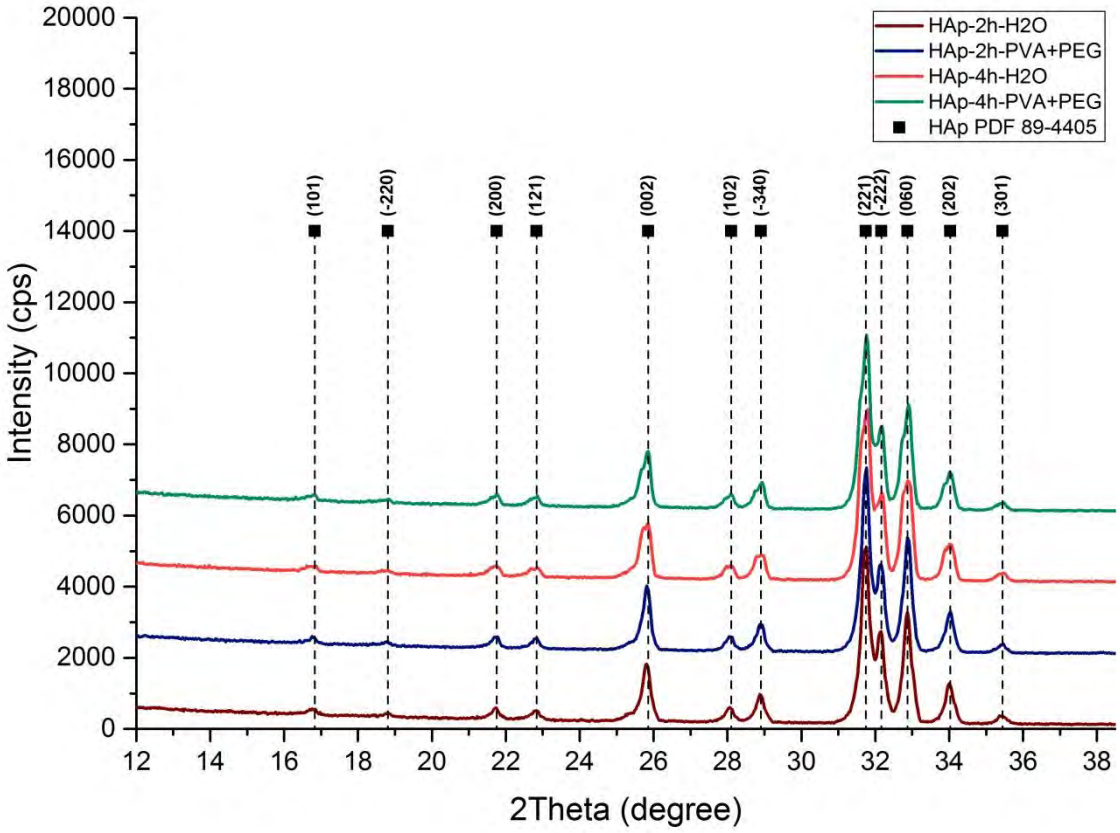

Figure 32: Diffraction peaks from the XRD patterns of the sintered targets

The results show that the structure of all the targets corresponds to that for monoclinic HAp. After sintering at 2 to 4 hours, and the addition of PVA and PEG, no changes are observed in the diffraction peaks from the XRD patterns. However, the targets that were sintered for 4 hours have a larger crystal size compared to the targets that were sintered for 2 hours, as shown in Table 12.

Table 12: Variation of crystal size and crystallinity of the HAp targets with 72 MPa at 1200 °C (2h, 4h / H_2O, PEG+PVA).

Target	Crystal size (nm)	Crystallinity (%)
72MPa, 2h, 1200 °C, H_2O	26.5	40
72MPa, 4h, 1200 °C, H_2O	28.1	41
72MPa, 2h, 1200 °C, PVA+PEG	26.4	39
72MPa, 4h, 1200 °C, PVA+PEG	27.6	40

Crystal size was calculated according to Scherrer equation:

$$T = \frac{K\lambda}{\beta cos\theta} \qquad (11)$$

Where T is the crystallite size, K is a dimensionless number of the order of unity, known as the Scherrer constant (1), λ is the wavelength of the radiation (in this case 0.05406 nm), β

is the width of the diffraction maximum measured at a height half-way between background and peak (in radians), and θ is the Bragg angle [68].

The crystallinity percentage was calculated applying the following equation using the Difrac.EVA software.

$$\frac{\text{(total}}{} \qquad \frac{\text{peaks)}}{} \qquad (12)$$

Densification and linear shrinkage

Tables, 13 and 14 show density comparison and linear shrinkage variation for targets with different additives respectively.

Table 13: Density behavior for HAp discs fabricated with 72 MPa at 1200 °C (2h, 4h / H_2O, PEG+PVA).

Target	Green density (g/cm^3)	Sintered density (g/cm^3)	Variation (%)	ρ (%)
2h, H_2O	1.33	1.61	21	51
4h, H_2O	1.33	1.69	27	54
2h, PEG+PVA	1.34	1.70	27	54
4h, PEG+PVA	1.34	1.78	33	56

Table 14: Linear shrinkage variation for targets with 72 MPa at 1200 °C (2h, 4h / H_2O, PEG+PVA).

Target	Green thickness (mm)	Sintered thickness (mm)	shrinkage (%)
2h, H2O	1.38	1.15	17
4h, H2O	1.38	1.10	20
2h, PEG+PVA	1.37	1.08	21
4h, PEG+PVA	1.37	1.04	24

These results show that the relative density and crystal size are influenced by the sintering time. The average of the crystal size increased in the range of 1.2 to 2.5 nm with increasing the sintering time. Meanwhile, the relative density ranged from 54% for the sample sintered for 2 hours, to 56% for the sample sintered for 4 hours. According to the literature, the grains have more time to grow for a longer sintering time, as a result, both the average grain size and relative density increased with increase of the sintering time [69].

It is also observed that the targets that were compacted with an additive system which consists of a binder (PVA) and a plasticizer (PEG) have a higher relative density. Similar observation was also reported in the literature, for a PVA-PEG additive system, the relative density increases as the percentages of binder increase for sintering at a given temperature [70].

Table 15: Composition of HAp sintered targets with 72 MPa at 1200 °C (2h, 4h / H_2O, PEG+PVA).

Element (At%)	**Powder**	**add + 2h**	**add + 4h**	**H_2O + 2h**	**H_2O + 4h**
C	6.15	5.36	5.55	4.82	5.23
O	50.05	48.47	50.05	46.83	48.3
Mg	0.28	0.35	0.30	0.00	0.04
P	16.56	16.92	16.71	16.86	16.58
Ca	26.96	28.90	27.39	31.49	29.86
Ratio					
Ca/P	1.628	1.708	1.639	1.868	1.801
O/Ca	1.856	1.677	1.827	1.487	1.618
O/P	3.022	2.865	2.995	2.778	2.913

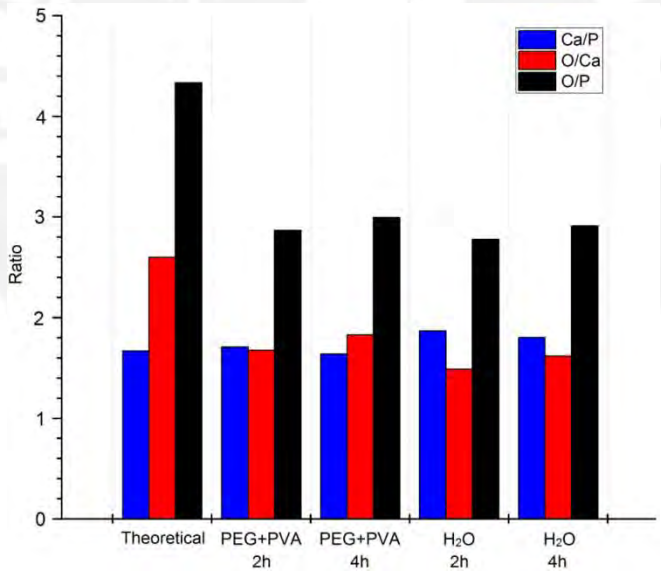

Figure 33: Comparison in ratios of the HAp targets with 72 MPa at 1200 °C (2h, 4h / H_2O, PEG+PVA). Theoretical ratios of HAp were added for a better view.

The results obtained with the EDX analysis are shown in Table 15 and in Figure 33. The results show a change in the atomic composition of HAp where the ratio Ca/P increases after sintering, this can be attributed to the partial decomposition of the hydroxyapatite as effect of the temperature (1200 °C). Decomposition of the HAp follows the equation [71]:

$$Ca_{10}(PO_4)_6(OH)_2 \rightarrow 3\ \beta - Ca_3(PO_4)_2 + Ca_4(PO_4)_2O + H_2O \qquad (13)$$

$$Ca_4(PO_4)_2O \rightarrow 4CaO + P_2O_5 \uparrow \quad (14)$$

HAp decomposes into TTCP ($Ca_4(PO_4)_2O$), tricalcium phosphate $\beta - TCP$ ($\beta - Ca_3(PO_4)_2$), phosphorus pentoxide(P_2O_5) and calcium oxide (CaO), as shown in equations B and C. This explains the loss of oxygen and phosphorus during sintering, since the boiling temperature of P_2O_5 is 360 °C. The diffraction peaks from the XRD patterns of the sintered targets do not show these species, this can be explained by assuming that they are in the amorphous state, since as it was previously described, the targets are not 100 % crystalline.

4.1.2 Scanning electron microscopy

Figure 34 shows the micrographs of the analyzed targets taken in the SEM, where the formation of characteristic necks of the sintering process is observed and the measured pore size is in a range of 0.5-1.2 µm.

After the analysis of all the results obtained, the target, which was compacted at 72 MPa with additive system (PVA+PEG) and sintered for 4 hours, was selected to perform the deposition on PMMA substrates because it has the highest relative density, the atomic composition is the one closest to the powders used for the manufacture, and it exhibits the representative peaks of the XRD pattern for monoclinic HAp.

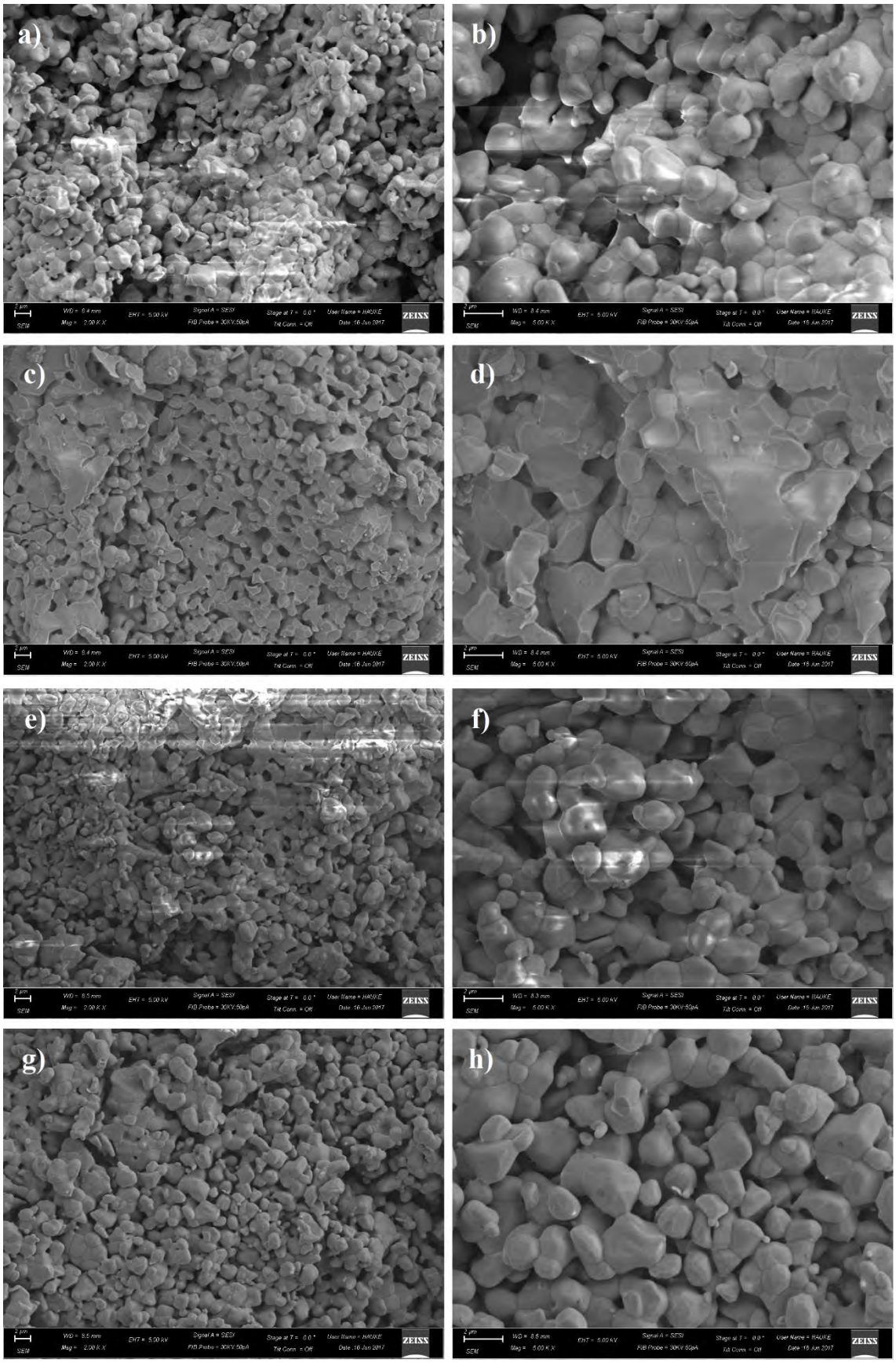

Figure 34: SEM micrographs for HAp targets sintered with 72 MPa and 1200 °C: a) & b) 2h, PEG+PVA; c) & d) 4h, PEG+PVA; e) & f) 2h, H_2O; g) & h) 4h, H_2O. Magnification: left images at 2.00 KX and right images at 5.00 KX. SEM images were taken after laser cut.

3.2 Thin film of calcium phosphates on PMMA substrates

3.2.1 XRD results

The calcium phosphates films, produced by RFMS and IBS on the substrates of PMMA printed with different infill percentages (60%, 70%, 80%, 90% and 100%), were analyzed by the XRD analysis technique as well as the uncoated PMMA substrate. The results are shown in **Figure 35**.

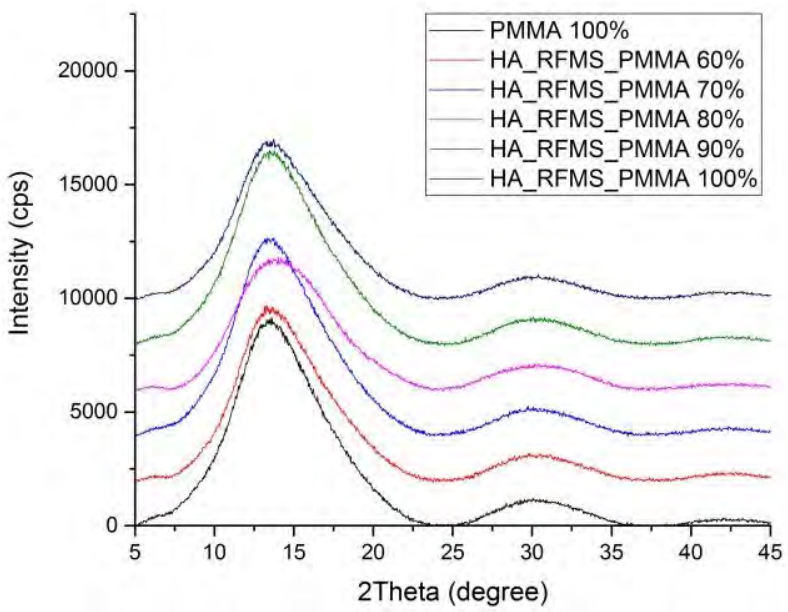

Figure 35: XRD patterns of PMMA substrates coated with calcium phosphate by RFMS

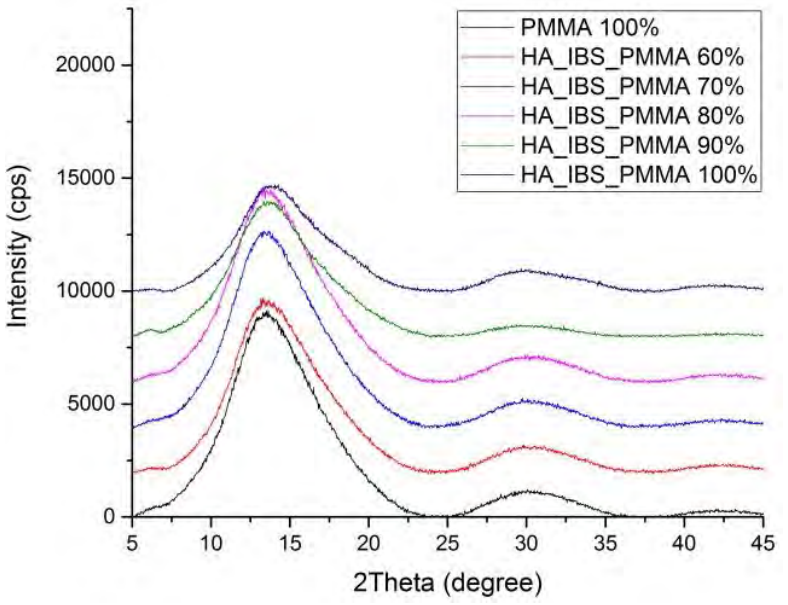

Figure 36: XRD patterns of PMMA substrates coated with calcium phosphate by IBS

The XRD diffraction scans exhibits for all the samples a characteristic broad amorphous hump observed around 2θ= 13.5°, 30.2° and also a weak hump observed at about 2θ= 42.2° [72].

No diffraction peak is observed in any of the samples, which indicates that the films deposited on PMMA by both methods, RFMS and IBS, are amorphous. In the interaction between X-rays with disordered atoms, X-rays will be scattered in many directions leading to a large bump distributed in a wide range (2 Theta) instead of high intensity narrower peaks, while, when there is periodic arrangement of atoms the X-rays will be scattered in certain directions forming high intensity peaks [73],[74].

3.2.2 **SEM results**

Figure 37 presents the micrographs of the PMMA substrate printed with 80% infill, before (a) and after (b) HAp deposition by RFMS. It can be observed that the HAp film adheres conformably to the substrate. A similar condition was observed for the same substrate with HAp films deposited by IBS (not shown here). There is no deleterious influence of the substrate surface on film deposition, although some general discontinuities are observed, such as some porosity, bubbles generated during filament extrusion, and heterogeneous roughness; all these discontinuities are typical in a FDM process [6].

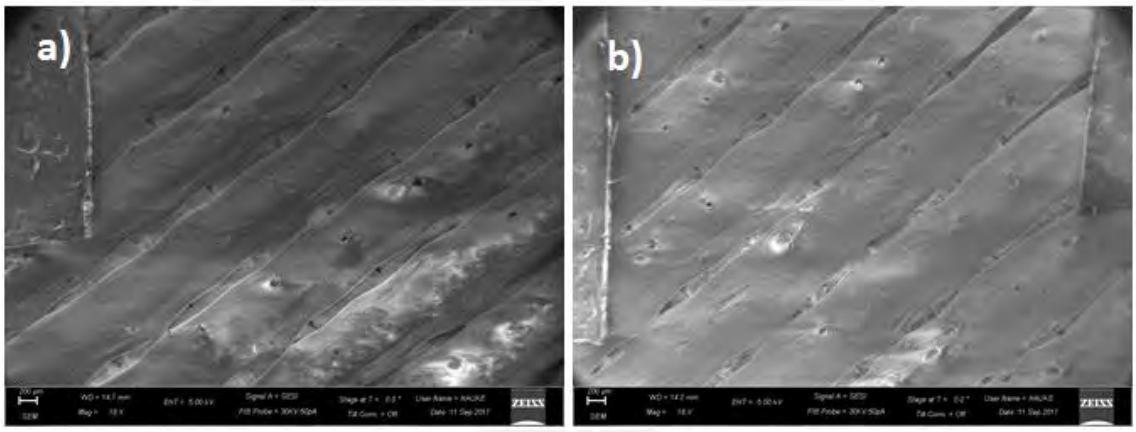

Figure 37: PMMA substrate, a) printed by FMD with 80% infill, b) printed by FMD with 80% infill and coated with 200 nm of amorphous calcium phosphate by RFMS (Mag =10 x)

Although no differences are observed macroscopically in the substrates, at the microscopic level the deposited calcium phosphate films can be observed. Figure 38.a shows the surface of the uncoated substrate, Figure 38.b, c and d show the micrographs of calcium phosphate films deposited by RFMS on the PMMA substrate with 100% infill (low porosity), 80% infill and 60 % infill (high porosity), respectively. It is observed in all cases, that the growth of the film is similar, confirming that there is no influence of the percentage of infill of the substrate on the growth of the film. A columnar micro-structure is observed.

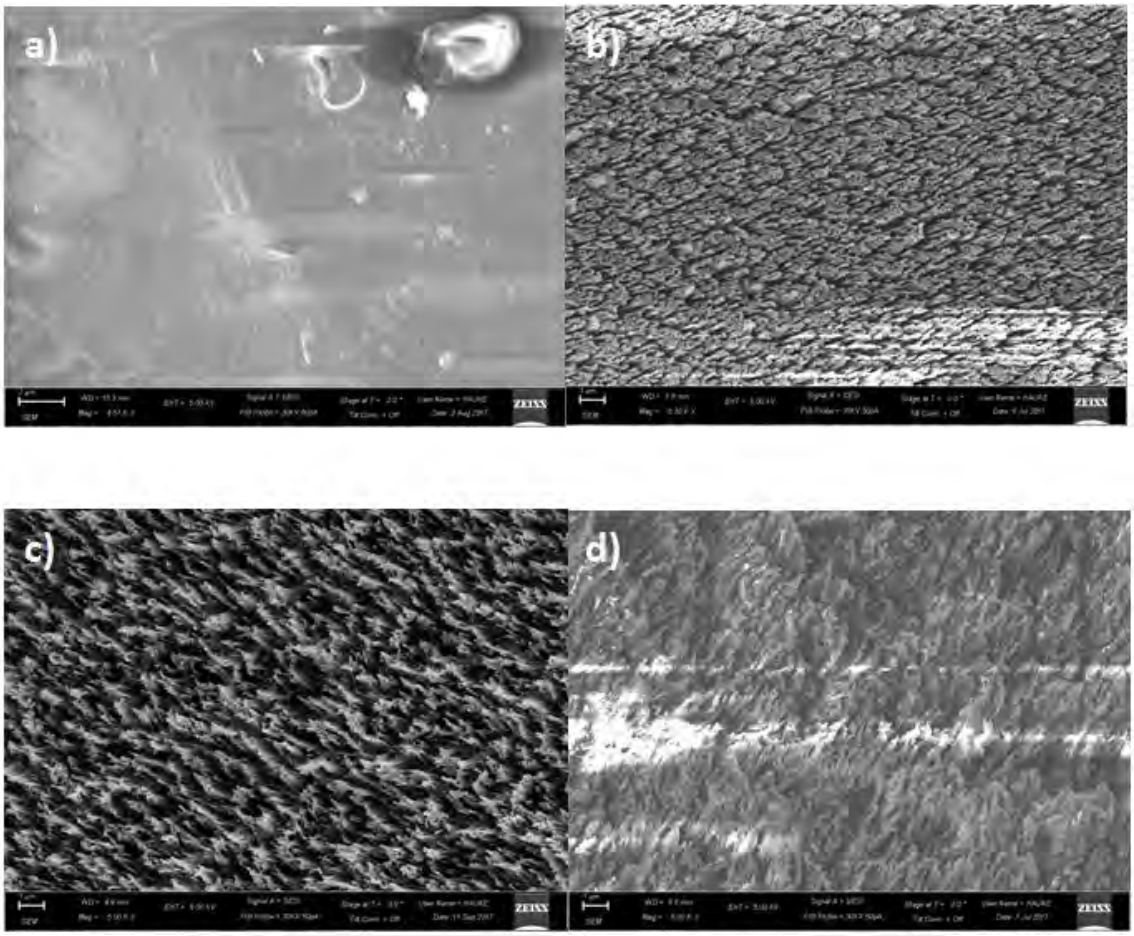

Figure 38: a) substrate of PMMA manufactured by FDM with 100% of infill, b), c) and d) substrates of PMMA, manufactured by FDM with 100%, 80% and 60% of infill respectively, coated by RFMS with a calcium phosphates film with a thickness of about 200 nm (Mag =18.0 KX)

The amorphous and columnar micro-structure can be attributed to some parameters of the process such as: temperature of the substrate, bias voltage applied to the substrate and density ionic current, as can be observed in the model presented by P.J. Kell and R.D. Arnell [29]. See Figure 39

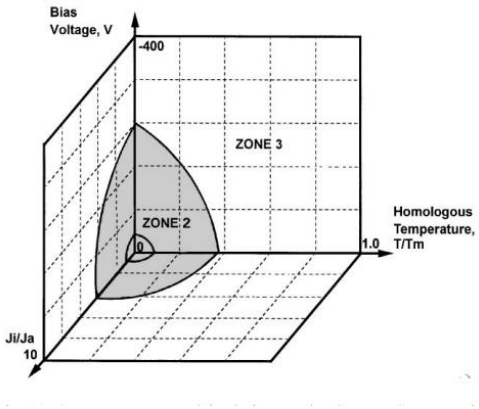

Figure 39: Structure zone model relating to the closed-field unbalanced magnetron sputtering (CFUBMS) system, in which structures are described in terms of homologous temperature (T/Tm), ion-to-atom current ratio (Ji/Ja) and bias voltage (v) [29]

This model was designed for an specific process, however it can be considered as a reference to observe the influence of the parameters mentioned above. In accordance with the model of J. Thornton [75], this model presents the relation between microstructure of the thin films and the normalized temperature, Ts/Tm (Ts is the temperature of the substrate and Tm is the melting temperature of the target or coating material) [29] [75]. Thornton zone model presents specific zones as is shown in Figure 40.

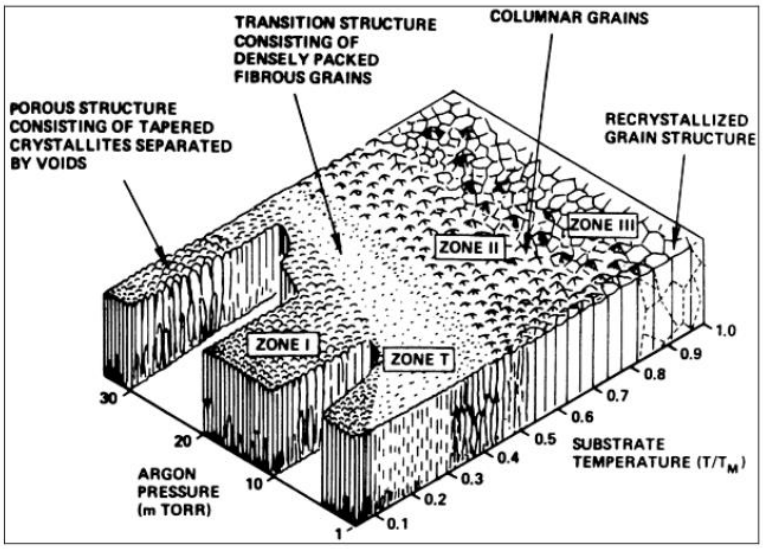

Figure 40: Thorton zone model [71]

In the present work, the calcium phosphate films were deposited at room temperature, it was about 25 °C, and the melting temperature of the HAp is 1660 °C. In this case the relation Ts/Tm is lower than 0.1, therefore it is in zone I of Thornton model [75]. This zone is formed by small and elongated grains that form a columnar structure with porous morphology, intergranular boundaries are voids rather than true grain boundaries; as a result of this the coatings have poor lateral strength and low density [75]. The columnar

structure at Ts/Tm <0.l, is produced by a low mobility of the atoms adsorbed by the substrate surface (adatom), low diffusion, and intergranular shading, which are produced by the varying velocity in the growth the columns and the various incidence angles at which the atoms arrive at the surface of the substrate [75][76]. At greater magnification, the columnar morphology of the film can be observed, the crystallites have diameters between 70 nm to 115 nm, as is shown in Figure 41.

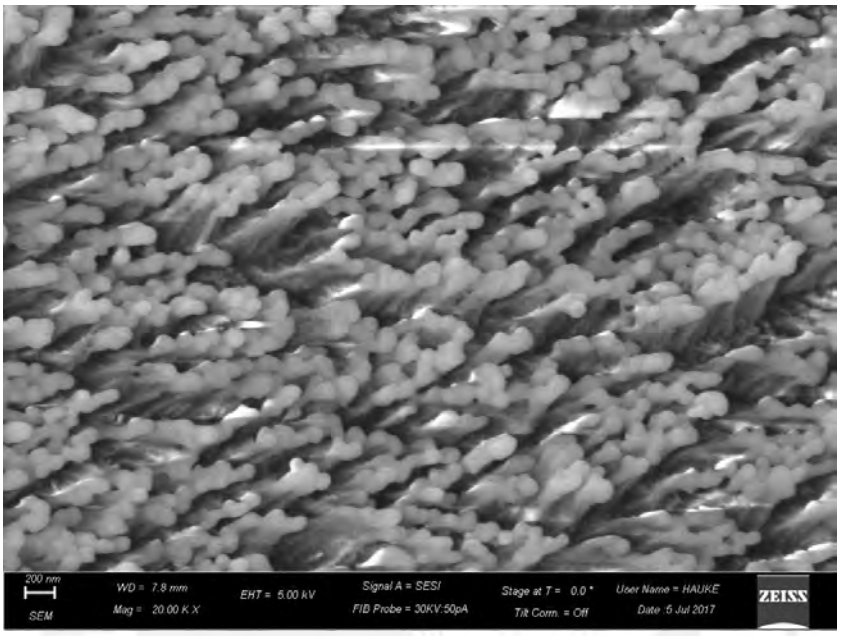

Figure 41: Columnar morphology of calcium phosphate thin film growth by RFMS on PMMA printed substrate (Mag =20.0 KX)

The bias voltage applied to the substrate has the same effect on the mobility and adsorption of the atoms as an increase in the temperature, so when it is increased, the T zone increases and the first zone decreases, resulting in denser thin films with a high degree of crystallinity [76]. In the deposition of the films in the present work no bias voltage was applied to the substrate.

The ionic current density drawn at the substrate is directly proportional to the ionic current density applied to the target, which depends of different parameters: gas flow, power, RFMS machine design, among others. The deposition rate is directly proportional to the ionic current density applied to the target [29]. If the two processes are compared, RFMS has a low deposition rate (0.56 nm/min) compared with IBS process, which has a rate deposition of 1.5 nm/min in this work, therefore the ionic current is lower in RFMS.

The films deposited by IBS also show an amorphous morphology, but the morphology of the film is less columnar, as is shown in Figure 42.

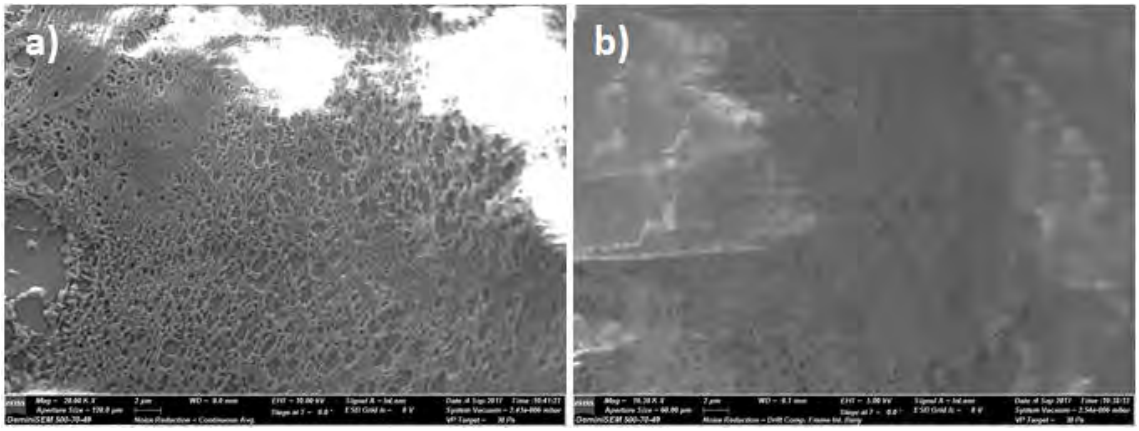

Figure 42: a) and b) Substrates of PMMA, manufactured by FDM with 100% and 60% of infill respectively, coated by IBS with calcium phosphates films with thickness about 300 nm (Mag =18.0 KX)

At greater magnification (Figure 43), the micro-structure of the film and the shape of the grains can be observed, the diameter of these grains are in the range of 120nm to 500 nm. Instead of densely standing columns with round heads RFMS, IBS produces ridges of standing platelets with curved contours.

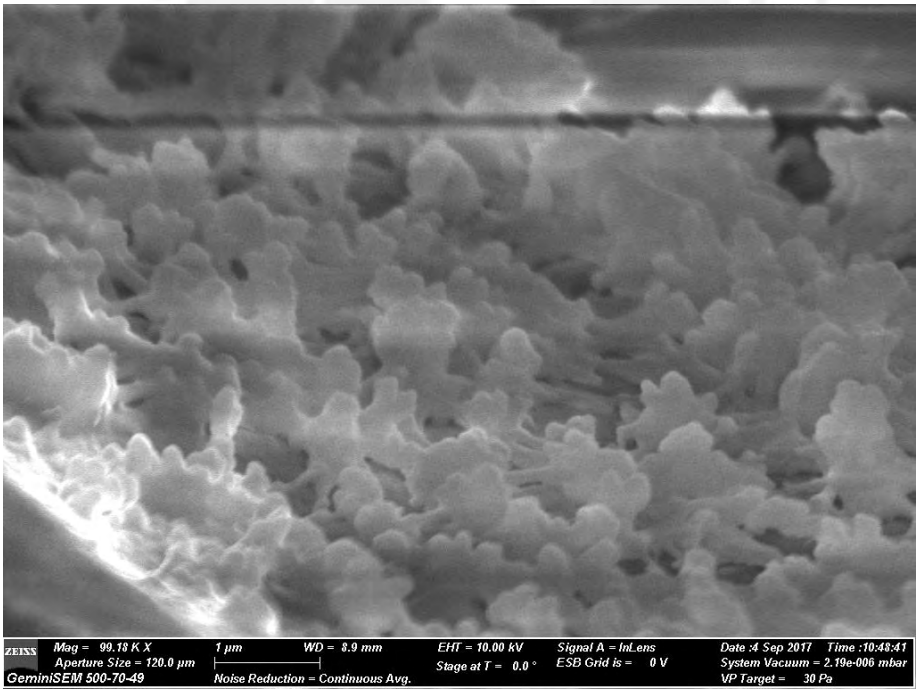

Figure 43: Morphology of calcium phosphate thin film growth by IBS on PMMA printed substrate

The difference can be attributed to the deposition rate of 1.5nm/min in IBS deposition, which is higher than 0.56 nm/min rate deposition of RFMS. In other investigations, the dependence of the morphology and grain size of the film on the deposition rate has been presented [77].

The deposition rate is related to the number of atoms that reach the surface of the substrate per unit time, therefore at higher deposition rates, the number of atoms onto the surface per unit time is higher. In this way the atoms arriving onto the substrate surface can diffuse along the surface and form clusters which can also contribute to the growth of grains. At low deposition rates, the surface diffusion of the atoms and formation of clusters is not prominent. Therefore the density of clusters, which can potentially coalesce to form grains, is small, therefore a small grain is formed [77]. In the present work, the diameter of the amorphous grains of the films deposited by IBS is greater than the diameter of the grains deposited by RFMS.

3.2.3 EDX results

The films deposited on the printed PMMA substrates were analyzed by EDX, the results of this analysis are shown in Table 16 and Table 17.

Table 16: EDX analysis results of films deposited by RFMS on printed PMMA substrates

Element (At%)	**100% infill**	**80% infill**	**60% infill**
C	70.75	69.72	68.72
O	25.92	26.66	27.41
Mg	0.16	00.0	0.09
P	1.16	1.17	1.33
Ca	2.27	2.33	2.37
Ratio			
Ca/P	1.95	1.98	1.78

Table 17: EDX analysis results of films deposited by IBS on printed PMMA substrates

Element (At%)	**100% infill**	**80% infill**	**60% infill**
C	39.89	27.12	36.74
O	43.15	37.55	43.44
Mg		0.00	0.00
P	4.84	6.51	4.90
Ca	12.12	28.82	14.91
Ratio			
Ca/P	2.51	4.42	3.04

The presence of carbon and excess of oxygen is due to the composition of PMMA. The Ca/P ratio of the films is in the range of 1.78 to 1.98, which is higher than the theoretical ratio of hydroxyapatite (1.67) and the composition of the target used.

The difference in the Ca/P ratio between the HAp target and the sputtering coatings has been attributed to the preferential deposition of positively charged radicals (CaO^{+}) and

ions (Ca^{+} and Ca^{2+}), and a possible significant loss of P ions ($(PO_4)^{3-}$ anions) generated in the plasma, which may be pumped away before reaching the substrate [78] . Other investigators have also reported the loss of P ions, suggesting that due to the loss of oxygen during sputtering (oxygen is easily pumped away) the phosphorus is weakly bound to the growing film and as a result is sputtered away by incoming ions or electrons [79][80].

In the analysis of films deposited by IBS a lower percentage of carbon is observed than in the films that were deposited by RFMS, this is because the films deposited by IBS are thicker therefore the substrate composition has less influence in the analysis. It is also shown that the Ca /P ratio for the films deposited by IBS is higher. This can be attributed to the fact that if the thickness of the film is greater the deposition of the positively charged ions or the loss of P ions will be greater.

3.2.4 Roughness results

The results of the roughness measurement are shown in Table 18

Table 18: Roughness measurements

	PMMA film	HA- PMMA Film by IBS	PMMA substrate Printed 100%	HA-PMMA Printed 100% by RFMS	HA-PMMA Printed 100% by IBS
Ra	28 nm	55 nm	765 nm- 987 nm	809 nm	1027 nm
Rz	143 nm	238 nm	3296 nm	3640 nm	4665 nm

The results show that the substrates manufactured by FDM have a high roughness in the range of 765 nm to 987 nm. After being coated with a film by RFMS or IBS of 200 and 300 nm respectively, there is no noticeable change in the roughness; this supports what was observed by SEM in terms that the films adheres conformably to the PMMA substrate.

To determine the roughness of the film produced by IBD a PMMA film with 28 nm roughness was coated. The roughness obtained from the film was 55 nm, the difference of surface roughness between substrate and coating is about 30 nm. Thornton explains that when the growth of the film is in zone 1, the substrate roughness is reproduced in exaggerated form on the coating surface [81]. Further research also shows that the roughness of the film deposited on a rough substrate is greater than the substrate roughness [82].

The roughness of the film is greater than the roughness of the substrate because a rough surface has a fluctuation in the surface energy, where the points of the peaks have greater energy than the valleys, for this reason it is easier to form nucleus in the points of peaks than in the valleys. Therefore, atoms diffuse and transfer to peak points on which coating grows preferentially. Coating grows slowly in valleys compared with peak points because it is harder to form nucleus and receive diffusing atoms at valleys. Finally, overlapping-island morphology is formed [82][83].

The morphology of the film is also related to the roughness of the substrate since Thornton zone model is designed for single phase materials on smooth substrates, where

Zone I terminates at T/Tm > 0.3. On rough substrates, Zone 1 boundaries persist to high values of T/Tm [81].

3.2.5 Hardness results

The results of the hardness test for the samples are shown in Figure 44. The hardness of the PMMA film is 220 Pa, the hardness of the substrate obtained by FDM is in the range of 217 to 378 Pa, the hardness obtained from the film that was deposited on the PMMA film is in the range of 2453 Pa to 2897 Pa, the results of the films that were deposited on the substrate obtained by FDM show lower values.

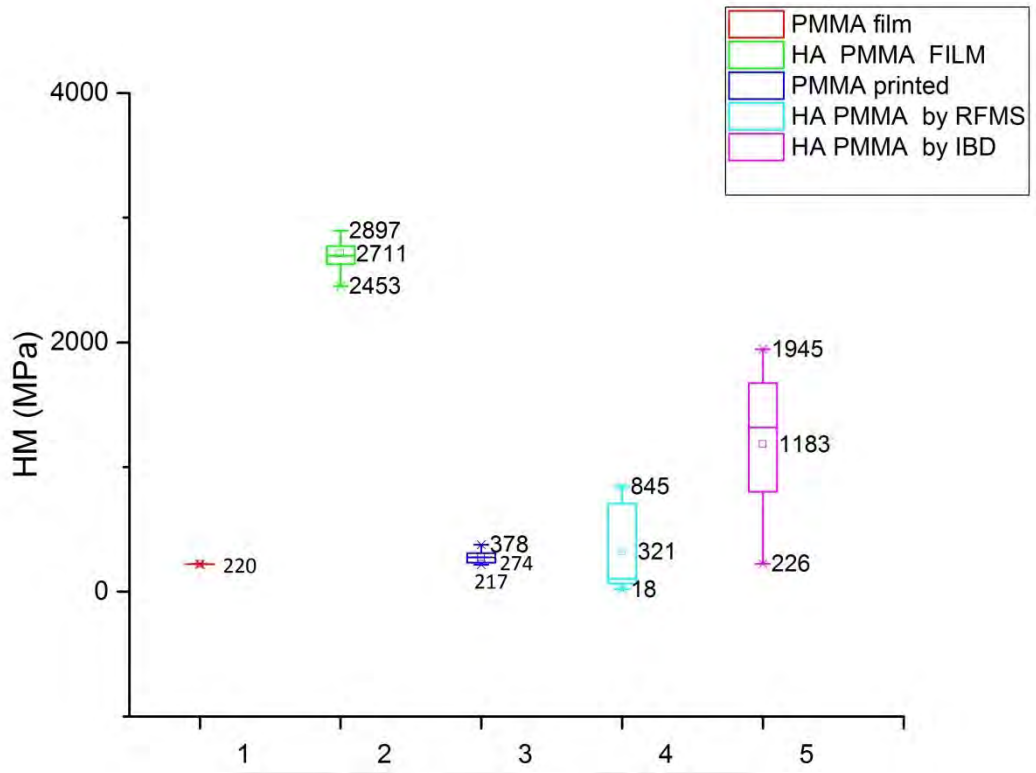

Figure 44: Hardness test results: on the x-axis the analyzed samples are distributed and on the y-axis the hardness values in MPa are show, for this 12 measurements were made per sample.

In other investigations the hardness of crystalline hydroxyapatite films produced by magnetron sputtering is in a range of 3.4 GPa–5 GPa [78][84]. In the present work the highest hardness was obtained in the film that was deposited by IBS (mean value = 2,7 GPa) on PMMA film. The low hardness of the films obtained is due to the amorphous morphology, since amorphous structures presents a smaller number of chemical bonds between the atomic clusters in contact than the crystalline structures. The irreversible deformation of crystalline and amorphous calcium phosphates follows the same mechanism the rupture of chemical bonds and the formation of new bonds. Therefore having fewer bonds to break when the film is amorphous translates into a significantly lower hardness [85].

The hardness obtained from the film deposited by IBS on PMMA printed substrate was lower than the hardness of the film deposited in the PMMA film. This can be attributed to

the effect of surface roughness on nano-indentation test, where the nano-hardness of rough thin films from nano-indentation tests is significantly lower than it predicted for smooth thin film [86]. As shown in section 4.2.4, the roughness of the film deposited on the PMMA substrate printed by FDM is much greater than that for the coating deposited on PMMA film, therefore, it is congruent with the effect of the roughness.

The film obtained by RFMS has a fairly low hardness compared to those previously mentioned. Can be observed in SEM micrographs, the low density of the films and it is directly related to hardness, at low densities low hardness [87].

4 Conclusions and Future work

4.1 Conclutions

A set of substrates have been fabricated from polymethyl methacrylate (PMMA) by means of 3D printing (FDM technique), with different infill percentage (60%, 80%, and 100%). These substrate surfaces have high roughness (Ra= 765 nm to 987 nm) and porosity. The porosity of the surface depends on the percentage of infill, the higher the infill the lower the porosity. In addition to these pores that are originated by the design of the substrate, pores that were generated by bubbles during the printing process by FMD were also evidenced.

A set of sputtering targets was fabricated from hydroxyapatite powders by the compaction and sintering process; the target with the best characteristics after the sintering process was compacted at 72 MPa and sintered for 4 hours at 1200 ^{o}C. This target had a relative density of 56% and a Ca/P ratio=1.64.

HAp films obtained by RFMS

Amorphous calcium phosphae films were grown by radiofrequency magnetron sputtering on PMMA printed substrates with different infill percentage, using a target of hydroxyapatite provided by Stanford Advanced Materials. The sputtering conditions for deposition were as follows: Work pressure around 6.7×10^{-3} mbar , Argon and Oxygen gas flow of 15 and 12 scc, respectively, 100 W power and a work pressure of around 6.7×10^{-3} mbar. Under these conditions the deposition rate was 0.56 nm/min .

The percentage of infill of the substrate shows no influence on the morphology of the film, substrates with 100%, 80% and 60% present the same characteristics; the pores on the substrate surfaces are in the order of the millimeters and the thickness of the deposited HA films is about 200-300 nm.

XRD analysis and SEM micrographs revealed the amorphous and columnar structure of the HA films, respectively, which is due to the low diffusion of the atoms in the substrate surface. The factors that contribute to the low diffusion of the atoms are: the high surface roughness, the low temperature of the substrate, a low ionic current density (related with the deposition rate, in this work is 0.56nm/min), and by not applying bias voltage

HAp films obtained by IBS

Amorphous calcium phosphate films were grown by ion beam sputtering (IBS) deposition on PMMA printed substrates with different infill percentage, using the manufactured target of hydroxyapatite. The sputtering conditions for deposition were as follows: Work pressure around $8x10^{-3}$ Pa, beam energy 4.6 KeV, right and left gun in a range of 310μA – 320 μA. With these parameters, a deposition rate of 1.5 nm/min was obtained.

XRD analysis and SEM micrographs of these films deposited by IBS also show an amorphous phase and a micro-structure with ridges of standing platelets with curved

contours different to the films deposited by RFMS. This can be attributed to the fact that the diffusion of the atoms on substrate surface is greater in this process due to a higher deposition rate, which determines the number of atoms in the surface per unit of time. Therefore at a higher deposition rate more atoms will be available on the surface which contributes to the formation of larger grains. This structure could be favorable since in some investigations it was concluded that the submicron scale of grains and pores on the surface are the properties which influence the increased osteo-conductivity in calcium phosphates [88].

The results of the EDX analysis of films deposited by RFMS and IBS show that the Ca/P ratio is higher than that for the stoichiometric hydroxyapatite and the targets used for deposition. This increase in the Ca/P ratio of the film with respect to the target can be explained by the preferential deposition of positively charged radicals (CaO^{+}) and ions (Ca^{+} and Ca^{2+}) during the process.

In the present work all the films produced have a Ca/P ratios >2, this result does not seem convenient, because in previous investigations it was demonstrated that in substrates with Ca/P ratios >2, the osteoblast viability decreased, and for Ca/P ratios <2, it was optimized, promoting osteoblast alkaline phosphatase activity [89]. Further cell culture tests are needed in order to elucidate osteoablast activity in the generated surfaces.

The lower roughness for the substrates produced by FDM is in the range of 765 nm-987 nm and measurements reveal that the roughness of the substrate is replicated in the film and is increased because the film grows faster in peaks compared with valleys, because it is easier to form nucleus and receive diffusing atoms at valleys because the peaks have more surface energy than the valleys. In previous investigations it was found that a roughness of about 900 nm is favorable for the implant incorporation in bone since for titanium implants in vitro studies revealed that rough surfaces (Ra about 900 nm) had much higher levels of osteoblast-like cells attached, than smoother surfaces (Ra about 30 nm) [90].

Results of hardness measurements show the lower hardness (0.27GPa) for the films deposited by RFMS on printed PMMA substrates due to the morphology of the film with a low density and high roughness. The highest hardness (2,7 GPa) was obtained from the film deposited on the PMMA substrate film deposited by IBS but the hardness of the film decreases to 1.18 GPa when the film is deposited on the printed PMMA substrate, confirming the roughness influence on the hardness measurements

4.2 Future work

More samples need to be prepared with more control over the process with the RFMS "homemade" equipment used at PUCP to fabricate the samples, in order to expand and support the results obtained in this investigation.

Furthermore, adhesion tests should be conducted in order to verify Thornton model prediction in terms of structure and adhesion properties [75].

The roughness produced during the manufacturing process of the substrate by MDF can be reduced by using acetone baths to polish the surface; however, it is necessary to study the change in PMMA microstructure after polishing and its influence for subsequent coating with HAp.

To continue with the long term objectives of this investigation it is necessary to conduct in vitro evaluation of the films to analyze the osteoinduction and the possible dissolution of the calcium phosphate coating in a biological media. Also it is necessary to find a methodology to avoid the loss of P and limit the increase of the Ca/P ratio, for this it could be necessary to vary the parameters of deposition of the films.

5 Bibliographic references

[1] A. L. Fernandes da Silva, A. M. Borba, N. R. Simão, F. L. M. Pedro, A. H. Borges, and M. Miloro, "Customized polymethyl methacrylate implants for the reconstruction of craniofacial osseous defects.," *Case Rep. Surg.*, vol. 2014, p. 358569, 2014.

[2] D. Espalin, K. Arcaute, D. Rodriguez, F. Medina, M. Posner, and R. Wicker, "Fused deposition modeling of patient-specific polymethylmethacrylate implants," *Rapid Prototyp. J.*, vol. 16, no. 3, pp. 164–173, 2010.

[3] W. A. Ribeiro Neto, A. C. C. de Paula, T. M. M. Martins, A. M. Goes, L. Averous, G. Schlatter, and R. E. Suman Bretas, "Poly (butylene adipate-co-terephthalate)/hydroxyapatite composite structures for bone tissue recovery," *Polym. Degrad. Stab.*, vol. 120, pp. 61–69, 2015.

[4] M. Maas, U. Hess, and K. Rezwan, "The contribution of rheology for designing hydroxyapatite biomaterials," *Curr. Opin. Colloid Interface Sci.*, vol. 19, no. 6, pp. 585–593, 2014.

[5] I. Navarro-Baena, M. P. Arrieta, A. Sonseca, L. Torre, D. Lopez, E. Gimenez, J. M. Kenny, and L. Peponi, "Biodegradable nanocomposites based on poly(ester-urethane) and nanosized hydroxyapatite: Plastificant and reinforcement effects," *Polym. Degrad. Stab.*, vol. 121, pp. 171–179, 2015.

[6] B. C. Gross, J. L. Erkal, S. Y. Lockwood, C. Chen, and D. M. Spence, "Evaluation of 3D printing and its potential impact on biotechnology and the chemical sciences," *Anal. Chem.*, vol. 86, no. 7, pp. 3240–3253, 2014.

[7] M. Asadi-Eydivand, M. Solati-Hashjin, A. Farzad, and N. A. Abu Osman, "Effect of technical parameters on porous structure and strength of 3D printed calcium sulfate prototypes," *Robot. Comput. Integr. Manuf.*, vol. 37, pp. 57–67, 2016.

[8] D. G. García, "Hydroxyapatite coatings: A comparative study between plasma-spray and pulsed laser deposition techniques," (PhD. Thesis), Dublin City University, 2009.

[9] A. Ragu, K. Senthilarasan, and P. Sakthivel, "Synthesis and Characterization of Nano Hydroxyapatite with Poly Vinyl Pyrrolidone Nano Composite for Bone Tissue Regeneration," *Int. J. Eng. Res. Appl.*, vol. 4, no. 10, pp. 50–54, 2014.

[10] A. Shavandi, D. A. Bekhit, Z. F. Sun, and A. Ali, "A Review of Synthesis Methods, Properties and Use of Hydroxyapatite as a Substitute of Bone," *J. Biomimetics, Biomater. Biomed. Eng.*, vol. 25, pp. 98–117, 2015.

[11] M. Swetha, K. Sahithi, A. Moorthi, N. Srinivasan, K. Ramasamy, and N. Selvamurugan, "Biocomposites containing natural polymers and hydroxyapatite for bone tissue engineering," *Int. J. Biol. Macromol.*, vol. 47, no. 1, pp. 1–4, 2010.

[12] M. Okada and T. Matsumoto, "Synthesis and modification of apatite nanoparticles for use in dental and medical applications," *Jpn. Dent. Sci. Rev.*, vol. 51, no. 4, pp. 85–95, 2015.

[13] Z. Evis and T. J. Webster, “Nanosize hydroxyapatite: doping with various ions,” *Adv. Appl. Ceram.*, vol. 110, no. 5, pp. 311–321, 2011.

[14] R. M. German, *Sintering from empirical observation to scientific principles*, First edit. Kidington, Oxfort, 2014.

[15] L. C. De Jonghe and M. N. Rahaman, *Sintering of Ceramics*, vol. 1–2. 2003.

[16] E. Champion, “Sintering of calcium phosphate bioceramics,” *Acta Biomater.*, vol. 9, no. 4, pp. 5855–5875, 2013.

[17] C. Yang, Y. kui Guo, and M. lin Zhang, “Thermal decomposition and mechanical properties of hydroxyapatite ceramic,” *Trans. Nonferrous Met. Soc. China (English Ed.*, vol. 20, no. 2, pp. 254–258, 2010.

[18] K. Tõnsuaadu, K. A. Gross, L. Pluduma, and M. Veiderma, “A review on the thermal stability of calcium apatites,” *J. Therm. Anal. Calorim.*, vol. 110, no. 2, pp. 647–659, 2012.

[19] S. F. Ou, S. Y. Chiou, and K. L. Ou, “Phase transformation on hydroxyapatite decomposition,” *Ceram. Int.*, vol. 39, no. 4, pp. 3809–3816, 2013.

[20] P. E. Wang and T. K. Chaki, “Sintering behaviour and mechanical properties of hydroxyapatite and dicalcium phosphate,” *J. Mater. Sci. Mater. Med.*, vol. 4, no. 2, pp. 150–158, 1993.

[21] V. Nelea, C. Morosanu, M. Iliescu, and I. N. Mihailescu, “Hydroxyapatite thin films grown by pulsed laser deposition and radio-frequency magnetron sputtering: Comparative study,” *Appl. Surf. Sci.*, vol. 228, no. 1–4, pp. 346–356, 2004.

[22] K. de Groot, J. G. CWolke, and J. A. and Jansen, “Calcium phosphate coatings for medical implants.,” *J. Eng. Med.*, vol. 212, no. 2, pp. 137–147, 1998.

[23] A. Vardelle, C. Moreau, N. J. Themelis, and C. Chazelas, “A Perspective on Plasma Spray Technology,” *Plasma Chem. Plasma Process.*, vol. 35, no. 3, pp. 491–509, 2015.

[24] M. Gindrat, H. M. Höhle, K. Von Niessen, P. Guittienne, D. Grange, and C. Hollenstein, “Plasma spray-CVD: A new thermal spray process to produce thin films from liquid or gaseous precursors,” *J. Therm. Spray Technol.*, vol. 20, no. 4, pp. 882–887, 2011.

[25] L. Besra and M. Liu, “A review on fundamentals and applications of electrophoretic deposition (EPD),” *Prog. Mater. Sci.*, vol. 52, no. 1, pp. 1–61, 2007.

[26] D.-M. Liu, Q. Yang, and T. Troczynski, “Sol–gel hydroxyapatite coatings on stainless steel substrates,” *Biomaterials*, vol. 23, no. 3, pp. 691–698, 2002.

[27] Y. Zhang, J. Tao, Y. Pang, W. Wang, and T. Wang, “Electrochemical deposition of hydroxyapatite coatings on titanium,” *Trans. Nonferrous Met. Soc. China*, vol. 16, no. 3, pp. 633–637, 2006.

[28] A. Bigi, E. Boanini, B. Bracci, A. Facchini, S. Panzavolta, F. Segatti, and L. Sturba, “Nanocrystalline hydroxyapatite coatings on titanium: A new fast biomimetic method,” *Biomaterials*, vol. 26, no. 19, pp. 4085–4089, 2005.

[29] P. Kelly and R. Arnell, “Magnetron sputtering: a review of recent developments and applications,” *Vacuum*, vol. 56, no. 3, pp. 159–172, 2000.

[30] L. W. Rieth, “Sputter Deposition of ZnO Films,” University of Florida, 2001.

[31] K. Ellmer, F. Kudella, R. Mientus, R. Schieck, and S. Fiechter, “Influence of discharge parameters on the layer properties of reactive magnetron sputtered ZnO:Al films,”

Thin Solid Films, vol. 247, no. 1, pp. 15–23, 1994.

[32] M.M.Abdelrahman, "Study of Plasma and Ion Beam Sputtering Processes," *J. Phys. Sci. Appl.*, vol. 5, no. 2, pp. 128–142, 2015.

[33] S. R. Paital and N. B. Dahotre, "Calcium phosphate coatings for bio-implant applications: Materials, performance factors, and methodologies," *Mater. Sci. Eng. R Reports*, vol. 66, no. 1–3, pp. 1–70, 2009.

[34] M. Samuelsson, "High power impulse magnetron sputtering under industrial conditions," (Ph. D. Thesis), Linkoping University, 2011.

[35] N. A. Trujillo, "Antibacterial effects of sputter deposited silver-doped Hydroxiapatite thin films," (Master thesis), Colorado State University, 2011.

[36] R. A. Surmenev, "A review of plasma-assisted methods for calcium phosphate-based coatings fabrication," *Surf. Coatings Technol.*, vol. 206, no. 8–9, pp. 2035–2056, 2012.

[37] M. (Technical U. of G.) Koleva, "Polymethyl Methacrylate (PMMA)," in *CAE DS – Injection Moulding Materials*, vol. 106, no. 10, 2016, pp. 58–62.

[38] S. Azevedo, L. Diéguez, P. Carvalho, J. O. Carneiro, V. Teixeira, E. Martínez, and J. Samitier, "Deposition of ITO Thin Films onto PMMA Substrates for Waveguide Based Biosensing Devices," *J. Nano Res.*, vol. 17, pp. 75–83, 2012.

[39] S. M. Zebarjad, "A Study on Mechanical Properties of PMMA/Hydroxyapatite Nanocomposite," *Engineering*, vol. 03, no. 08, pp. 795–801, 2011.

[40] V. Jaiganesh, A. A. Christopher, and E. Mugilan, "Manufacturing of PMMA cam shaft by rapid prototyping," *Procedia Eng.*, vol. 97, pp. 2127–2135, 2014.

[41] J. Parthasarathy, "3D modeling, custom implants and its future perspectives in craniofacial surgery," *Ann. Maxillofac. Surg.*, vol. 4, no. 1, p. 9, 2014.

[42] B. Leukers, H. Gülkan, S. H. Irsen, S. Milz, C. Tille, M. Schieker, and H. Seitz, "Hydroxyapatite scaffolds for bone tissue engineering made by 3D printing," *J. Mater. Sci. Mater. Med.*, vol. 16, no. 12, pp. 1121–1124, 2005.

[43] G. Staffa, A. Barbanera, A. Faiola, M. Fricia, P. Limoni, R. Mottaran, B. Zanotti, and R. Stefini, "Custom made bioceramic implants in complex and large cranial reconstruction: A two-year follow-up," *J. Cranio-Maxillofacial Surg.*, vol. 40, no. 3, 2012.

[44] A. Villanueva, "Desarrollo de armazones (scaffolds) a partir de poli(ácido láctico) (PLA) y polietilenglicol (PEG) utilizando la técnica de modelado por deposición fundida (FDM) empleada en impresión 3D,"(Master Thesis), Pontificia Universidad Catolica del Peru, 2016.

[45] E. S. Velasco, "Scanning Electron Microscope (SEM) as a means to determine dispersibility," (Ph. D. Thesis), Iowa State University, 2013.

[46] G. H.Michler, *Electron Microscopy of Polymers*, no. 1. Halle, Germany: Springer Laboratory, 2014.

[47] R. Feidenhans'l, *Surface structure determination by X-ray diffraction*, vol. 10, no. 3. North-Holland, Amsterdam: Elsevier Science Publishers B.V, 1989.

[48] J. A. Seibert, "X-Ray Imaging Physics for Nuclear Medicine Technologists. Part 1: Basic Principles of X-Ray Production*," *J Nucl Med Technol*, vol. 32, pp. 139–147,

2004.

[49] Zakhia Moore, "Application of X-ray Diffraction Methods and Molecular Mechanics Simulations to Structure Determination and Cotton Fiber Analysis," University of New Orleans in, 2008.

[50] R. Jenkins, *X-ray Fluorescence Spectrometry*, 2nd editio. New York: Wiley-Interscience, 1999.

[51] B. D. Cullity and S. R. Stock, *Elements of X-Ray Diffraction*, Third Edit. London - England: Pearson Educated Limited, 2014.

[52] L. Alexander and H. P. Klug, "Determination of crystallite size with the x-ray spectrometer," *J. Appl. Phys.*, vol. 21, no. 2, pp. 137–142, 1950.

[53] B. Jönsson and S. Hogmark, "Hardness measurements of thin films," *Thin Solid Films*, vol. 114, no. 3, pp. 257–269, 1984.

[54] A. Iost and R. Bigot, "Hardness of coatings," *Surf. Coatings Technol.*, vol. 80, no. 1–2, pp. 117–120, 1996.

[55] C. Oliver and M. Pharr, "An improved technique for determining hardness and elastic modulus using load and displacement sensing indentation experiments," *Journal of Materials Research*, vol. 7, no. 11. pp. 1564–1583, 1992.

[56] S.-R. Jian, G.-J. Chen, J. S.-C. Jang, and Y.-S. Lai, "Nanomechanical properties of AlN(103) thin films by nanoindentation," *J. Alloys Compd.*, vol. 494, no. 1–2, pp. 219–222, 2010.

[57] W. C. Oliver and G. M. Pharr, "Measurement of hardness and elastic modulus by instrumented indentation: Advances in understanding and refinements to methodology," *J. Mater. Res.*, vol. 19, no. 01, pp. 3–20, 2004.

[58] F. Roudet, D. Chicot, X. Decoopman, A. Iost, J. Bürgi, J. Garcia-Molleja, L. Nosei, and J. Feugeas, "Modeling of very thin aluminum nitride film mechanical properties from nanoindentation measurements," *Thin Solid Films*, vol. 594, pp. 129–137, 2015.

[59] J. Peters, K. H, S. Imgc, and H. S. Chuo, "Contribution of ClRP to the Development of Metrology and Surface Quality Evaluation during the last fifty years," *System*, 1970.

[60] N. L. Johnson, "On the comparison of estimators.," *Biometrika*, vol. 37, no. 3–4, pp. 281–287, 1950.

[61] E. S. Gadelmawla, M. M. Koura, T. M. A. Maksoud, I. M. Elewa, and H. H. Soliman, "Roughness parameters," *J. Mater. Process. Technol.*, vol. 123, no. 1, pp. 133–145, 2002.

[62] K. Manas, E. Svoboda, and R. Devorakova, "Measuring of surface structure and their analysis (Report)," Czech Republic, 2009.

[63] A. Al-tounsi, "Effect of sintering parameters on the mechanical and physical properties of sinter formed materials," Doublin city university, 1992.

[64] J. C. Elliott, P. E. Mackie, and R. A. Young, "Monoclinic Hydroxyapatite,", *Science.*, vol. 13, pp. 7–10, 2005.

[65] G. Ma and X. Y. Liu, "Hydroxyapatite: Hexagonal or monoclinic," *Cryst. Growth Des.*, vol. 9, no. 7, pp. 2991–2994, 2009.

[66] R. M. German, "Green body homogeneity effects on sintered tolerances," *Powder Metall.*, vol. 47, no. 2, pp. 157–160, 2004.

[67] H. Buchkremer and N. Menzler, *Ceramic processing and sintering*, Second Edi. 2007.

[68] J. I. Langford and A. J. C. Wilson, "Scherrer after sixty years: A survey and some new results in the determination of crystallite size," *J. Appl. Crystallogr.*, vol. 11, no. 2, pp. 102–113, 1978.

[69] Q. B. Wang, Q. G. Wang, and C. X. Wan, "Effect of sintering time on the microstructure and properties of inorganic polyphosphate bioceramics," *Sci. Sinter.*, vol. 42, no. 3, pp. 337–343, 2010.

[70] C. N. Jaafar, I. Zainol, S. Sulaiman, and M. I. Ayub, "Effects of PVA-PEG binders system on microstructure and properties of sintered alumina," *Appl. Mech. Mater.*, vol. 564, pp. 355–360, 2014.

[71] A. G. Azevedo, K. Strecker, and H. F. Gorgulho, "Efeito da temperatura em processos de sinterização de pós de hidroxiapatita (Effect of temperature in process of sintering of hydroxyapatite powders)," *Cerâmica*, vol. 61, pp. 52–59, 2015.

[72] E. M. Abdelrazek, A. M. Hezma, A. El-khodary, and A. M. Elzayat, "Spectroscopic studies and thermal properties of PCL/PMMA biopolymer blend," *Egypt. J. Basic Appl. Sci.*, vol. 3, no. 1, pp. 10–15, 2016.

[73] R. Oswald, E. Kasper, and K. H. Gaukler, "A multiple scattering theory of elastic electron backscattering from amorphous surfaces," *J. Electron Spectros. Relat. Phenom.*, vol. 61, no. 3–4, pp. 251–274, 1993.

[74] E. Shobhana, "X-Ray Diffraction and UV-Visible Studies of PMMA Thin Films," *Int. J. Mod. Eng. Res.*, vol. 2, no. 3, pp. 1092–1095, 2012.

[75] J. A. Thornton, "Influence of apparatus geometry and deposition conditions on the structure and topography of thick sputtered coatings," *J. Vac. Sci. Technol.*, vol. 11, no. 4, pp. 666–670, 1974.

[76] J. O. and G. C. Edgar Alfonso, "Thin Film Growth Through Sputtering Technique and Its Applications," *J. Electron. Mater.*, vol. 23, no. 7, pp. 11–12, 1977.

[77] K. Bordo and H. G. Rubahn, "Effect of deposition rate on structure and surface morphology of thin evaporated al films on dielectrics and semiconductors," *Medziagotyra*, vol. 18, no. 4, pp. 313–317, 2012.

[78] R. Surmenev, A. Vladescu, A. Ivanova, M. Braic, R. Surmenev, A. Vladescu, I. Grubova, A. Ivanova, and M. Braic, "Radio Frequency Magnetron Sputter Deposition as a Tool for Surface Modification Implants," Intech, 2016, pp. 1–35.

[79] L. J. J. Betty, *Thin Calcium Phosphate Coatings for Medical Implants*, Bern, Switzerland, pp. 9–21, 2009.

[80] K. Vandijk, H. Schaeken, J. Wolke, and J. Jansen, "Influence of annealing temperature on RF magnetron sputtered calcium phosphate coatings," *Biomaterials*, vol. 17, no. 4, pp. 405–410, 1996.

[81] J. A. Thornton, "High rate thick film growth," *Ann Rev Mat Sci*, vol. 7, pp. 239–260, 1977.

[82] R. X. Huang, Z. B. Qi, P. Sun, Z. C. Wang, and C. H. Wu, "Influence of substrate roughness on structure and mechanical property of TiAlN coating fabricated by cathodic arc evaporation," *Phys. Procedia*, vol. 18, pp. 160–167, 2011.

[83] G. S. Bales and A. Zangwill, "Macroscopic model for columnar growth of amorphous films by sputter deposition," *J. Vac. Sci. Technol. A Vacuum, Surfaces, Film.*, vol. 9, no.

1, pp. 145–149, 1991.

[84] V. Nelea, C. Morosanu, M. Iliescu, and I. N. Mihailescu, “Microstructure and mechanical properties of hydroxyapatite thin films grown by RF magnetron sputtering,” *Surf. Coatings Technol.*, vol. 173, no. 2–3, pp. 315–322, 2003.

[85] V. M. Ievlev, A. V. Kostyuchenko, B. M. Darinskii, and S. M. Barinov, “Hardness and microplasticity of nanocrystalline and amorphous calcium phosphate coatings,” *Phys. Solid State*, vol. 56, no. 2, pp. 321–329, 2014.

[86] W. G. Jiang, J. J. Su, and X. Q. Feng, “Effect of surface roughness on nanoindentation test of thin films,” *Eng. Fract. Mech.*, vol. 75, no. 17, pp. 4965–4972, 2008.

[87] P. Juliet, K. Koski, J. Ho, and J. Holsa, “Properties of aluminium oxide thin films deposited by reactive magnetron sputtering,” *Thin Solid Films*, vol. 339, no. 1–2, pp. 240–248, 1999.

[88] W. Habraken, P. Habibovic, M. Epple, and M. Bohner, “Calcium phosphates in biomedical applications: Materials for the future?,” *Mater. Today*, vol. 19, no. 2, pp. 69–87, 2016.

[89] H. Liu, H. Yazici, C. Ergun, T. J. Webster, and H. Bermek, “An in vitro evaluation of the Ca/P ratio for the cytocompatibility of nano-to-micron particulate calcium phosphates for bone regeneration,” *Acta Biomater.*, vol. 4, no. 5, pp. 1472–1479, 2008.

[90] A. Wennerberg, “The Role of Surface Roughness for Implant Incorporation in Bone,” vol. 9, no. 1, 1999.

[91] M. Strickstrock, H. Rothe, S. Grohmann, G. Hildebrand, I. M. Zylla, and K. Liefeith, “Influence of surface roughness of dental zirconia implants on their mechanical stability, cell behavior and osseointegration,” *BioNanoMaterials*, vol. 18, no. 1–2, pp. 1–10, 2017.